



**AFRL-OSR-VA-TR-2013-0010**

## **Reconfigurable Cellular Photonic Crystal Arrays (RCPA)**

**Ali Adibi**

**Georgia Tech Research Corporation**

**March 2013**

**Final Report**

**DISTRIBUTION A: Approved for public release.**

**AIR FORCE RESEARCH LABORATORY  
AF OFFICE OF SCIENTIFIC RESEARCH (AFOSR)  
ARLINGTON, VIRGINIA 22203  
AIR FORCE MATERIEL COMMAND**

**REPORT DOCUMENTATION PAGE****Form Approved**  
**OMB No. 0704-0188**

Public reporting burden for this collection of information is estimated to average 1 hour per response, including the time for reviewing instructions, searching data sources, gathering and maintaining the data needed, and completing and reviewing the collection of information. Send comments regarding this burden estimate or any other aspect of this collection of information, including suggestions for reducing this burden to Washington Headquarters Service, Directorate for Information Operations and Reports, 1215 Jefferson Davis Highway, Suite 1204, Arlington, VA 22202-4302, and to the Office of Management and Budget, Paperwork Reduction Project (0704-0188) Washington, DC 20503.

**PLEASE DO NOT RETURN YOUR FORM TO THE ABOVE ADDRESS.****1. REPORT DATE** (DD-MM-YYYY)  
07-12-2012**2. REPORT DATE**  
Report Type - Final**3. DATES COVERED** (From - To)  
July 1, 2009-September 30, 2012**4. TITLE AND SUBTITLE**  
Reconfigurable Cellular Photonic Crystal Arrays (RCPA)**5a. CONTRACT NUMBER****5b. GRANT NUMBER**  
FA9550-09-1-0572**5c. PROGRAM ELEMENT NUMBER****6. AUTHOR(S)**  
Dr. Ali Adibi**5d. PROJECT NUMBER**  
2106AXB**5e. TASK NUMBER****5f. WORK UNIT NUMBER****7. PERFORMING ORGANIZATION NAME(S) AND ADDRESS(ES)**  
Georgia Tech Research Corporation  
505 10<sup>th</sup> Street NW  
Atlanta, GA 30332-0001**8. PERFORMING ORGANIZATION  
REPORT NUMBER****9. SPONSORING/MONITORING AGENCY NAME(S) AND ADDRESS(ES)**  
Air Force Office of Scientific Research  
875 North Randolph Street  
Arlington, Virginia 22203**10. SPONSOR/MONITOR'S ACRONYM(S)**  
AFOSR**11. SPONSORING/MONITORING  
AGENCY REPORT NUMBER**  
AFRL-OSR-VA-TR-2013-0010**12. DISTRIBUTION AVAILABILITY STATEMENT**  
Distribution A: Approved for Public Release**13. SUPPLEMENTARY NOTES****14. ABSTRACT**

This AFOSR-supported research was started in July 2009 and is directed toward the development of a new technology platform for optical and microwave signal processing based on reconfigurable integrated optics devices. This technology has the potential to revolutionize the design circle of optical and high frequency RF systems by providing a common platform for a diverse range of applications. We expect that the impact of the proposed platform in the related fields to be similar to that of field programmable gate arrays (FPGAs) on digital signal processing and digital IC design.

The main idea behind RCPA's design is to implement a multi-input multi-output (MIMO) optical processing block that can be adjusted to realize any desired transfer function matrix that lies within the limits defined by the system specifications. The proposed architecture for the RCPA is based on tunable cross-connected element matrices at the input and output and an array of processing unit cells. The proposed architecture will be realized on silicon-on-insulator (SOI) platforms by using coupled micro-resonator and waveguide structures as primary building elements. The basic tunability in the device will be implemented using tunable phase-shifter and couplers based on the thermo-optic effect and free carrier injection. To achieve this goal, in what follows, different steps (including theoretical and modeling tools development, microcavity fabrication and characterization techniques, and methods to develop chip-scale devices) will be presented in detail, with the idea being to address the several challenges before the realization of RCPA chips in both the architecture and device level. Our research in this field has already resulted in a number of scientific publications and technical presentations. A complete list of journal papers and conference presentations is included at the end of this report. AFOSR support has been acknowledged in all these publications and presentations.

# INSTRUCTIONS FOR COMPLETING SF 298

15. SUBJECT TERMS

16. SECURITY CLASSIFICATION OF:

17. LIMITATION OF  
ABSTRACT

18. NUMBER  
OF PAGES

19a. NAME OF RESPONSIBLE PERSON

a. REPORT

b. ABSTRACT

c. THIS PAGE

19b. TELEPHONE NUMBER *(Include area code)*

**Final Report to the  
Air Force Office of Scientific Research (AFOSR)**

# **RCPA: Reconfigurable Cellular Photonic Array**

Georgia Institute of Technology

***Principal Investigator:***

**Ali Adibi**

*Professor, School of Electrical and Computer Engineering,  
Georgia Institute of Technology  
Atlanta, GA 30332-0250  
e-mail: [adibi@ee.gatech.edu](mailto:adibi@ee.gatech.edu)  
Tel: (404) 385-2738  
Fax: (404) 894-4641*

Nov, 2012

## **I. Introduction**

This progress report summarizes achievements in Dr. Adibi's research group at Georgia Institute of Technology in the area of Reconfigurable cellular photonic arrays, supported by award grant number FA9550-09-1-0572 since July 2009. Only major achievements from July 2011 till November 2012 with very brief description are listed in this report. Detailed information can be found in the recent publications or can be directly requested from Dr. Adibi. A summary highlighting the most important achievements prior to July 2011 is also provided.

This AFOSR-supported research was started in July 2009 and is directed toward the development of a new technology platform for optical and microwave signal processing based on reconfigurable integrated optics devices. This technology has the potential to revolutionize the design circle of optical and high frequency RF systems by providing a common platform for a diverse range of applications. We expect that the impact of the proposed platform in the related fields to be similar to that of field programmable gate arrays (FPGAs) on digital signal processing and digital IC design.

The main idea behind RCPA's design is to implement a multi-input multi-output (MIMO) optical processing block that can be adjusted to realize any desired transfer function matrix that lies within the limits defined by the system specifications. The proposed architecture for the RCPA is based on tunable cross-connected element matrices at the input and output and an array of processing unit cells. The proposed architecture will be realized on silicon-on-insulator (SOI) platforms by using coupled micro-resonator and waveguide structures as primary building elements. The basic tunability in the device will be implemented using tunable phase-shifter and couplers based on the thermo-optic effect and free carrier injection. To achieve this goal, in what follows, different steps (including theoretical and modeling tools development, microcavity fabrication and characterization techniques, and methods to develop chip-scale devices) will be presented in detail, with the idea being to address the several challenges before the realization of RCPA chips in both the architecture and device level. Our research in this field has already resulted in a number of scientific publications and technical presentations. A complete list of journal papers and conference presentations is included at the end of this report. AFOSR support has been acknowledged in all these publications and presentations.

## II. Summary of Previous Research

### II.A. Novel microheater architecture for ultra-fast reconfiguration

In this new architecture, the microheater is placed directly on the Si surface of the microdisk towards the center and away from the resonator mode. As a result of high thermal conductivity of crystalline Si, heat propagation delay can be considerably reduced. Figures I(a) and I(b) show the simulated temperature profile at vertical and horizontal cross-sections of a  $5\mu\text{m}$ -radius microdisk. The volume of the microdisk is almost equi-temperature as a result of high thermal conductivity of Si. Figure I(c) shows the simulated normalized impulse response of this device. Heat propagation delay is observed to be 25ns which implies that close to 25ns reconfiguration time is possible using appropriate pulse-shaping of the excitation signal. The rise-time of this device is around  $3\mu\text{s}$ . The device is fabricated on a SOI wafer with a BOX thickness of  $1\mu\text{m}$ .

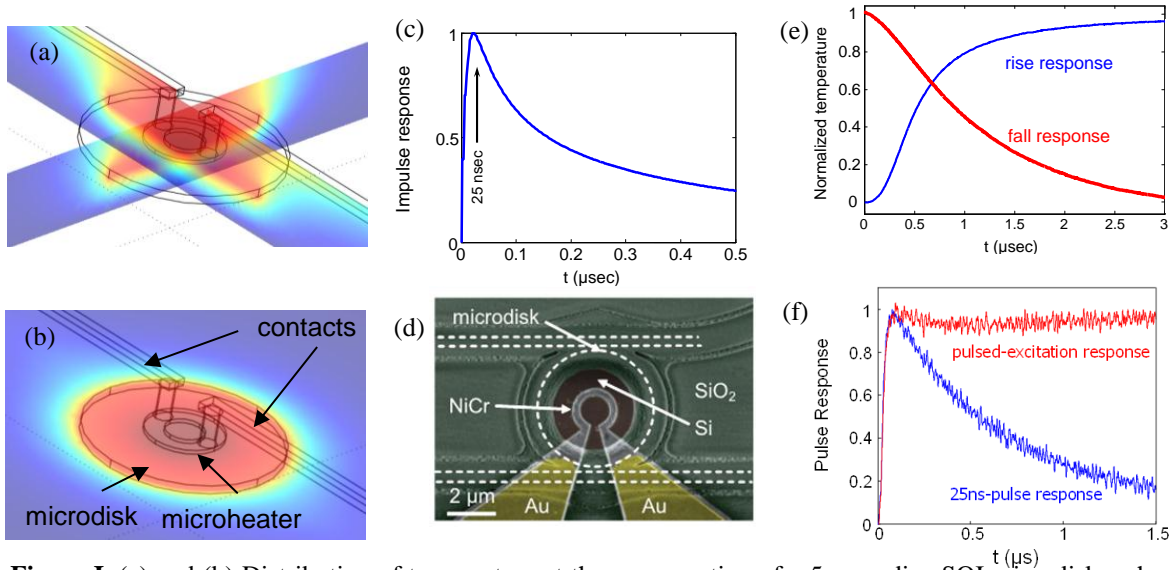


**Figure I.** (a) and (b) Distribution of temperature at the cross-section of a  $5\mu\text{m}$ -radius SOI microdisk as heat is generated in the metallic microheater. (c) Impulse response of the heater integrated on the disk. (d) SEM of the fabricated microheater over the  $5\mu\text{m}$ -radius microdisk. (e) Rise and fall responses of the corresponding microheater. (f) Normalized impulse response of the same heater.

After etching the photonic device in Si and covering it with PECVD SiO<sub>2</sub>, a window at the center of the microdisk is opened using ZEP resist. Resist is then reflowed on hot-plate at  $150^\circ\text{C}$  for 4 minutes, so that the sidewalls of the SiO<sub>2</sub> cladding which is etched afterwards have a roughly  $45^\circ$  angle. This tilted sidewall is necessary to connect heaters to the contacts outside the microdisk. After this step, heaters and contacts are defined through lift-off. Figure I(d) shows the SEM of one such device. The step response of this microheater is then measured. The blue and red curves in Figure I(e) show the rise and fall response of the microheater, respectively. Rise-time and fall-time are measured to be  $1.38\mu\text{s}$  and  $2.87\mu\text{s}$ , respectively. Also, a resonance wavelength shift of  $1.55\text{ nm/mW}$  is observed for this device. Figure I(f) shows the normalized impulse response of this device. The heat propagation delay is measured to be 75ns. This is because of the high thermal-contact resistivity between the surface of Si and the heater: Si surface is etched in the process of etching the SiO<sub>2</sub> cladding as a result of variation in the etch rate. This etching of Si is polymerizing and the top surface of Si will thus be contaminated. This problem can be fully mitigated by appropriate control over the etch rate.

## II.B. Reconfigurable wavelength convertor using compact coupled resonators

A simple traveling-wave resonator (TWR) has a fundamental design challenge for nonlinear optics applications. This issue rises from the fact that the field enhancement in the resonator is inversely proportional to the size of the resonator that is itself determined from the free-spectral range (FSR) that is needed to for the interacting signals. Therefore, for the typical FSRs that are needed from many interconnect and fiber optics systems (a few to tens of nanometer), large microresonators with small field-enhancement properties are used. We propose a new concept for designing coupled-resonator devices that enables us to design the resonance modes independently from the size of the structure. By over-coupling the resonators in a coupled-resonator structure, the supermodes split where the amount of splitting is determined by the amount coupling. Figure II(a) schematically shows a three-element coupled-resonator structure that is used in this work to demonstrate wavelength conversion through four-wave mixing (FWM) in Si. As seen in Figure II(b) mode splitting increases with the mutual coupling between the resonators and therefore, it is possible to design this structure for a degenerate FWM where the frequency difference of the pump and signal/idler waves is solely determined by the coupling coefficient and not the length of the resonators. The simulation result of the field-enhancement shows simultaneous enhancement at all the three split modes, which is the condition required for an efficient nonlinear interaction. This structure also opens the door for the possibility of the reconfiguration of the spacing between the resonance modes for the implementation of a tunable nonlinear optics process in a resonator-based device. This can be achieved both through the tuning of the coupling coefficients between the resonators and the resonance wavelengths of the individual resonators. We have experimentally tested the performance of the proposed device by fabricating a coupled-racetrack resonator on a SOI platform. Figure III(a) shows the optical micrograph of the fabricated device, and Figure III(b) shows its normalized transmission spectrum. The details of the FWM characterization setup are shown in Figure III(c). We measured the power of the idler at the output for a range of input pump powers and the results are shown by the red dots in Figure III(d). We also theoretically calculated the wavelength conversion in this device and the results are shown by the blue curve in Figure III(d). One of the unique features of the demonstrated device is the reconfigurability of the signal/idler wavelengths, while keeping the pump resonance exactly at the center of these modes, as shown by the red curve in Figure III(b).

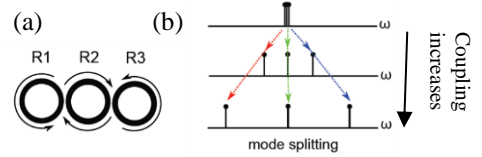


**Figure II.** (a) Schematic of a coupled-resonator device (b) Schematic characteristic of mode splitting in this device.

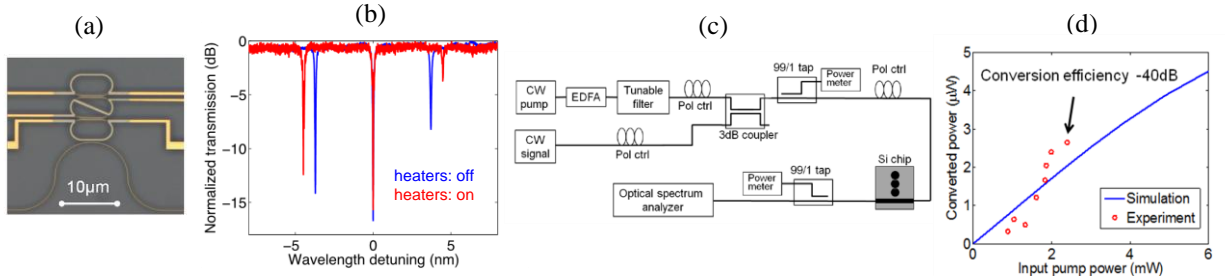


**Figure III.** (a) Optical micrograph of the coupled-resonator device. (b) Transmission spectrum of the device. (c) Experimental setup for FWM characterization. (d) Theoretical and experimental results for the idler power at the output versus the input pump power when the input signal power is 0.25mW.

### III. Research Accomplishments

#### III.A. Design and fabrication of an accumulation-mode modulator

Figure 1(a) shows the schematic of a compact resonator on the double-Si layer material platform discussed in section II.G. In the vertical direction, the structure is mainly a capacitor formed between two Si layers with a 50-nm thick  $\text{SiO}_2$  layer in between. In this structure, two separate electrodes are connected to the upper and lower Si layers to form electrical contacts to the two sides of the device capacitor. The modulator electrodes are connected toward the center of the microdisk resonator to assure their minimal overlap with the resonant mode of the microdisk. Figure 1(b) shows the distribution of the accumulated free-carriers (electrons and holes) in the lower and upper Si layers under a 4 V bias voltage between the two device electrodes, simulated using Sientaurus™ software. It is observed that the accumulated carriers in the top and bottom Si layers are concentrated within a few tens of nm of the dielectric layer. Since the total accumulated charge is linearly proportional to the applied voltage, the conductance of the device can be tuned through a DC bias voltage. This is illustrated in the simulation results in Figure 1(c) which shows the step response of the modulator to a 3 V signal at 4 V (blue curve) and 8 V (red curve) DC bias voltage. It is observed that the response time for the 8 V bias is twice as fast as the 4 V case because of the higher device conductance (lower RC). The response time of 15 ps achieved with 8 V bias is almost three times smaller than that in the best reported modulators using depletion-mode PN junctions [1]. This enables us to adaptively control the RC time constant of the device for different speed conditions. This is the unique advantage of the proposed device as compared to PN-junction modulators in which the conductivity is pre-determined by the doping level of impurities. At the same time, this eliminates the need for extra fabrication processes for defining the P and N regions, which reduces the cost and complexity of the device. One minor issue is to have a low-resistance connection from the modulator contacts to the accumulated free carriers at the two capacitor plates.

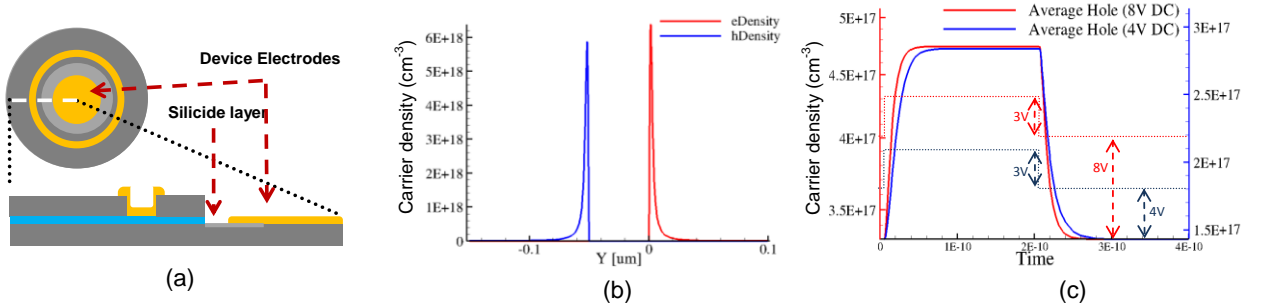
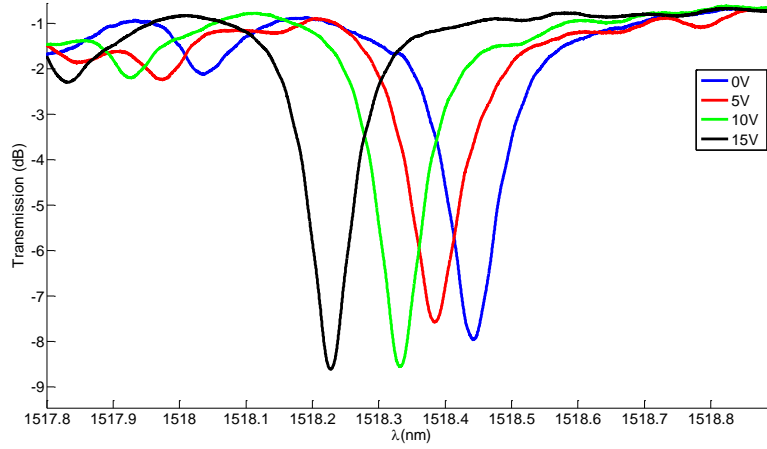


**Figure 1.** (a) Top image and cross-section of the proposed modulator device. The isolator layer in this case is a 50 nm-thick  $\text{SiO}_2$  film. (b) The distribution of the accumulated free-carriers (electrons and holes) at the two sides of the isolator layer in the proposed modulator for a bias voltage of 4 V. (c) The variation in the average concentration of holes (and electrons) in the modulator by applying a pulse voltage with an amplitude of 3V for two different bias voltages.

Figure 2 shows the preliminary experimental result from the actual fabricated device in which the disk radius was 30  $\mu\text{m}$ . The top and bottom silicon layers were 120 nm in thickness each with



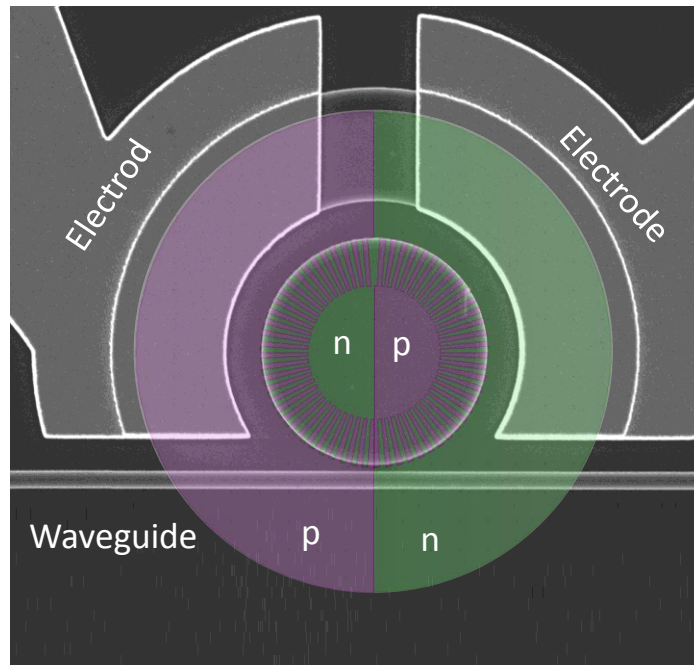
60 nm of SiO<sub>2</sub> in between. By applying a DC voltage to the structure the resonance frequency undergoes a blue shift due to carrier accumulation near the surfaces of the SiO<sub>2</sub> layer.



**Figure 2.** Electro-optical characteristic of the first fabricated accumulation-based device, showing the resonance wavelength of the resonator at different voltages. The blue shift of the resonance is due to carrier accumulation resulting from the applied voltage.

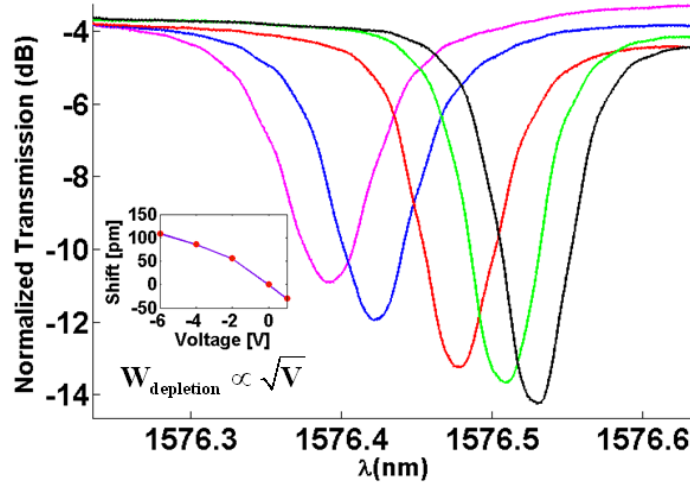
### III.B. Design and fabrication of PN junctions

Figure 3 show the SEM image of the 3  $\mu\text{m}$ -radius disk resonator in proximity to a waveguide and the electrodes. Also the doping profile of the resonator structure is super-imposed on the image. The p and n doping levels have both been chosen to be  $10^{18} \text{ cm}^{-3}$ . The structure has undergone a rapid thermal annealing for 15 seconds at 1050°C and 15 minutes at 900°C to achieve electrical activation.



**Figure 3.** SEM Image of a disk resonator coupled to its adjacent waveguide and the gold electrodes. The green and violet regions show the p-n profile.

Figure 4 shows the optical characterization result of the device. The resonance wavelength changes as the reverse voltage is applied and the pn region is depleted. Obviously the magnitude of the blue shift is not linear with the applied voltage because of the square root dependence of depletion width to the reverse bias. The inset in Figure 4 shows the square root dependence of this blue shift.

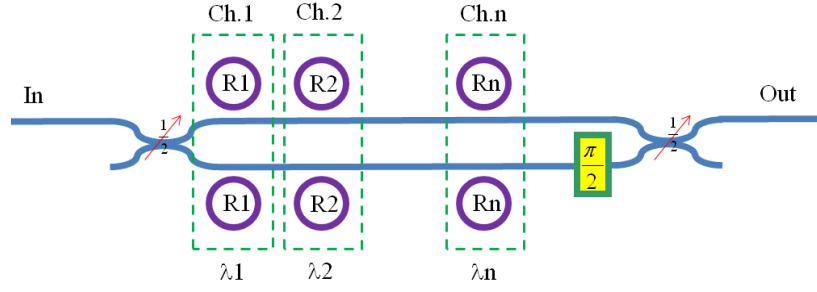


**Figure 4.** Optical characteristics of the pn-junction-based modulator in the reverse-biased (depletion) regime.

Here due to the special doping profile (pnpn) the needed voltage is twice that of simple pn doping. At the same time this choice of doping facilitates the fabrication process in the sense that the electrical via needed to reach to the center of the resonator in the simple pn profile is totally eliminated.

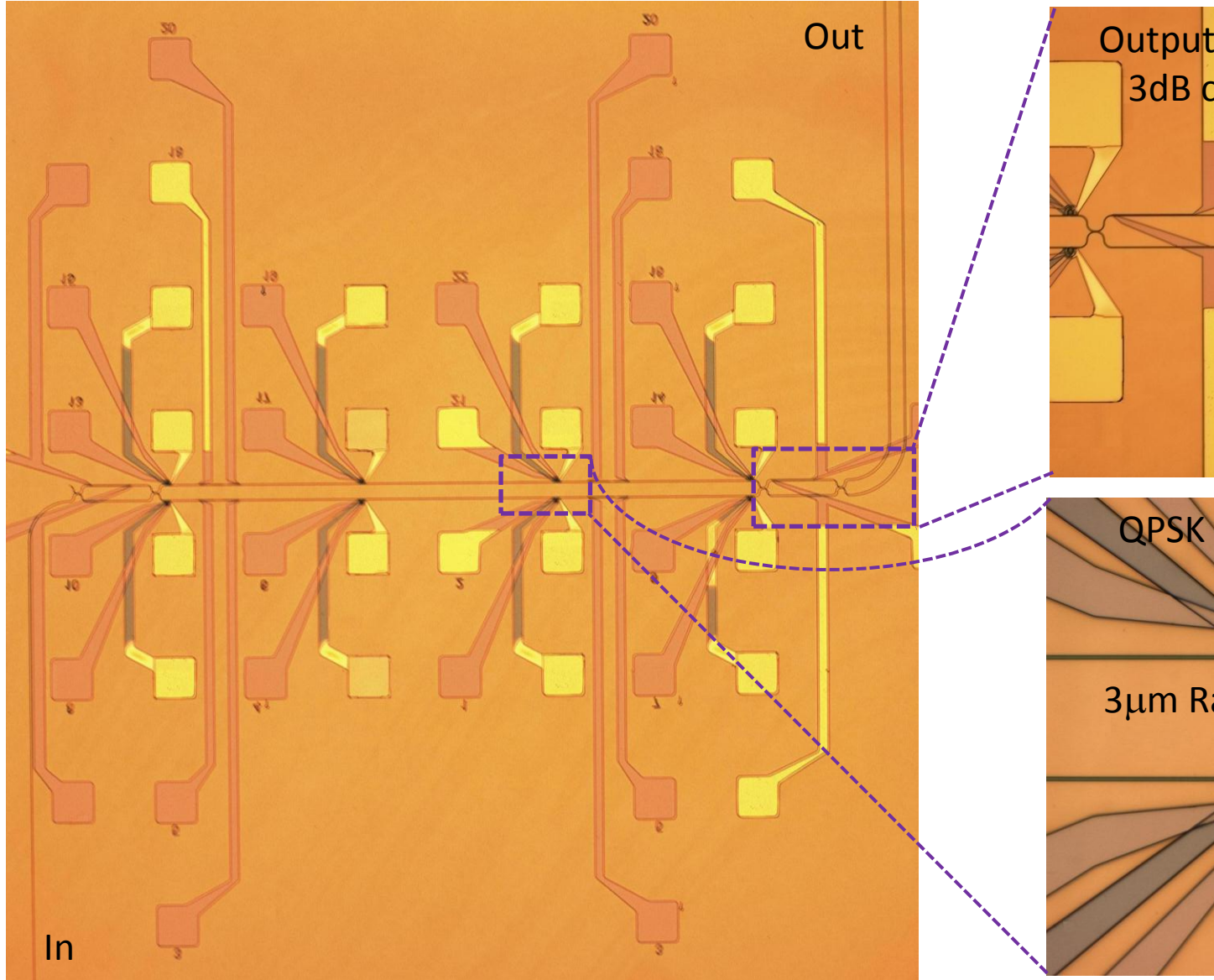
### III.C. Design and fabrication of a resonator-based QPSK modulator

Figure 5 shows the schematic of our proposed n-channel DQPSK modulator [2]. The structure is composed of a Mach-Zehnder interferometer (MZI) with 3dB couplers at two ends. Arrays of high quality factor (high- $Q$ ) resonators are coupled to the upper and lower arms. Each modulator channel is composed of a set of two resonators on the upper and lower MZI arms, tuned to the same resonance wavelength. These resonators provide the required in-phase (I) and quadrature-phase (Q) phase modulation for the corresponding DQPSK channel. The coupling of the resonators to the MZI waveguides is adjusted to achieve over-coupling and minimize the modulator insertion loss. The multi-channel DQPSK modulator is implemented by integrating an array of resonator pairs to the same MZI structure, each tuned to a different spectral channel.



**Figure 5.** Schematic diagram of a multi-channel DQPSK optical modulator

The proposed multi-channel modulator, therefore, needs to be excited by an input composed of  $N$  distinct tones at different wavelengths (i.e., a frequency comb input). The signal in each channel is conveyed onto the carrier using the corresponding pair of resonators (as shown with the dashed boxes in Figure 5). A wideband phase shift of  $\pi/2$  is embedded in the lower arm of MZI corresponding to the Q-phase. The phase modulation can be achieved through modulating the resonance wavelengths of the resonators by integrating a PN-junction for carrier injection or by thermal tuning for low speed modulation. A set of microheaters are used to adjust the center wavelengths of the resonators in the modulator structure.



**Figure 6.** Optical micrographs of the fabricated four-channel QPSK optical modulator.

Figure 6 shows the micrograph of the fabricated QPSK modulator with four channels. The input and output 3dB couplers are also tunable to make sure that the laser light divides equally between the arms of the Mach-Zehnder.

The fabrication flow is as follows: We start off with a standard SOI wafer and thin the top Si layer down to 240nm through thermal oxidation. Then through a round of Electron Beam Lithography (EBL) the passive optical devices are defined and etched in an ICP dry etching tool. The p-n regions are created by As<sup>+</sup> and BF<sub>2</sub><sup>+</sup> implantation. After rapid thermal annealing for electrical activation, electrical pads are defined and then the whole chip is spin-coated with flowable oxide (FOX<sup>TM</sup>-16) for passivation. Lastly, the heaters are implemented on top of the FOX layer and over the resonators through a Ti lift-off process.

The SEM in Figure 7-left shows the heater on top of the resonator. The blue curve in Figure 7-middle right shows the output signal at zero bias for heaters. As can be seen in this figure instead of 4 dips there are 8 dips in the transmission response that correspond to 8 different resonances.

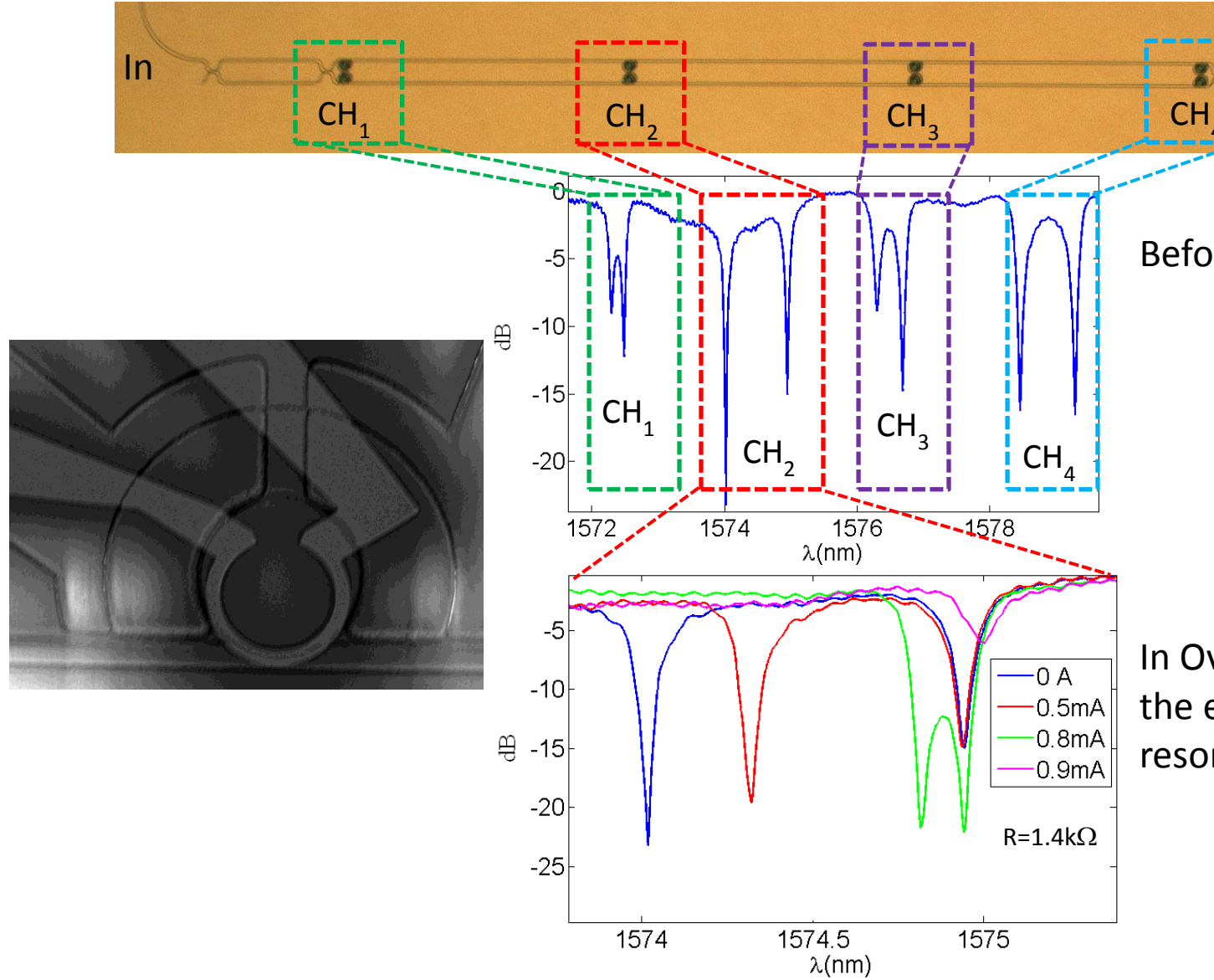


**Figure 7.** SEM and thermal tuning characteristics of the second channel of the QPSK modulator.

This is usually a result of fabrication inaccuracies that cause the resonators in each channel to be not perfectly identical. In Figure 7-lower right the transmission signal around the second channel with the resonances tuned to their designed positions is shown. The tuning was achieved by applying a DC current to the heater. The total pad-to-pad heater resistance was measured to be 1.4K ohm.

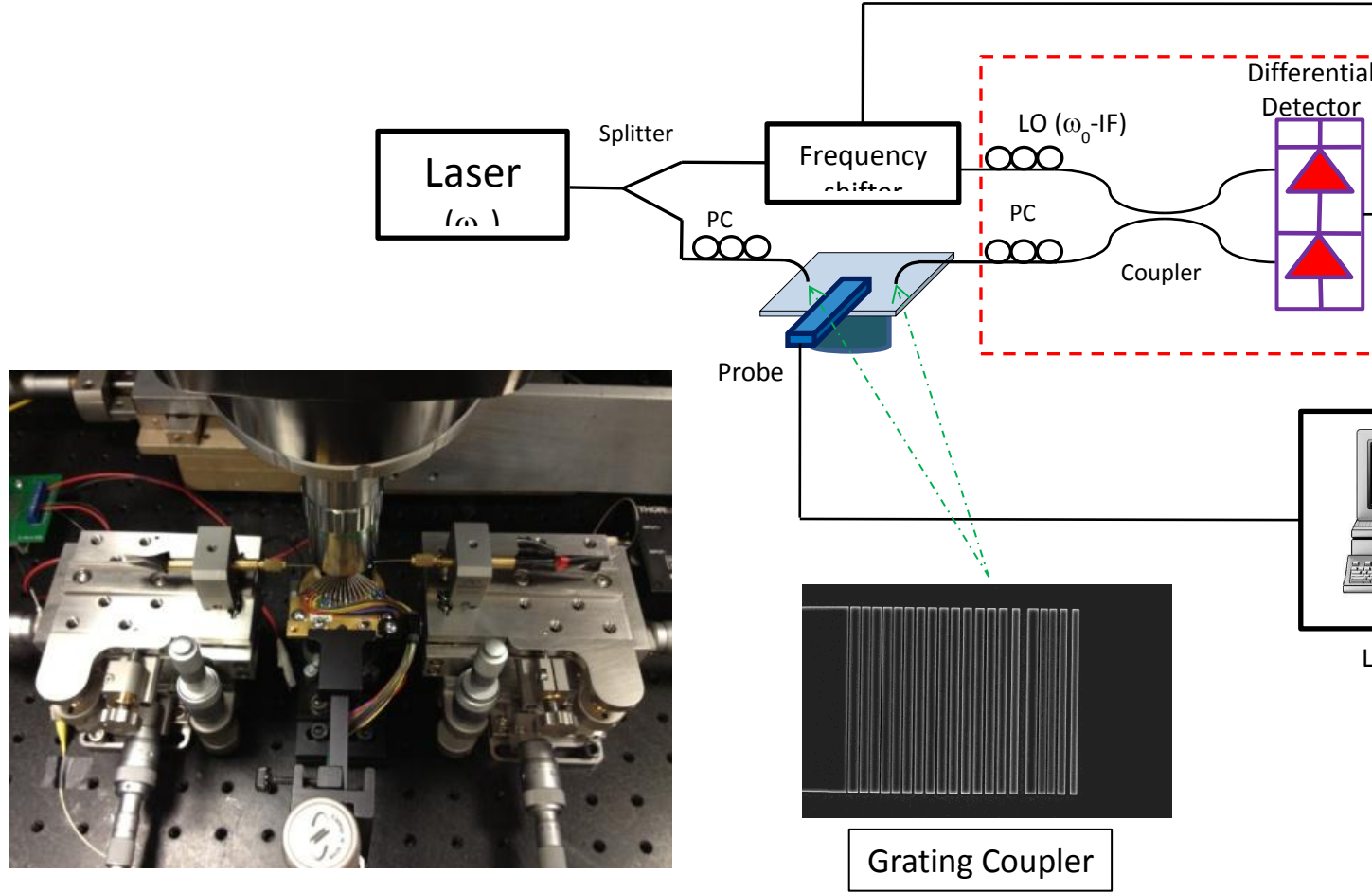


**Figure 8.** Characterization setup used for the low speed test of the QPSK modulator.

Figure 8 shows the characterization setup. The electrical signals needed for data modulation and calibration come to the pads through a probe controlled by a PC. The laser light comes in and splits into two branches. Laser light in the lower branch is coupled directly to the chip through a grating coupler after its polarization is adjusted by a polarization rotator. The signal is then picked up from the output coupler and fed to the coherent heterodyne demodulator. The wavelength of the laser light in the upper branch is shifted using a frequency shifter driven by the same signal as the intermediate frequency (IF) of the demodulator. The in-phase and quadrature components of the detected signal are then fed and processed in a PC using the Labview™ toolkit. An in-house code is developed and used to control the electrical signals and process the collected data.



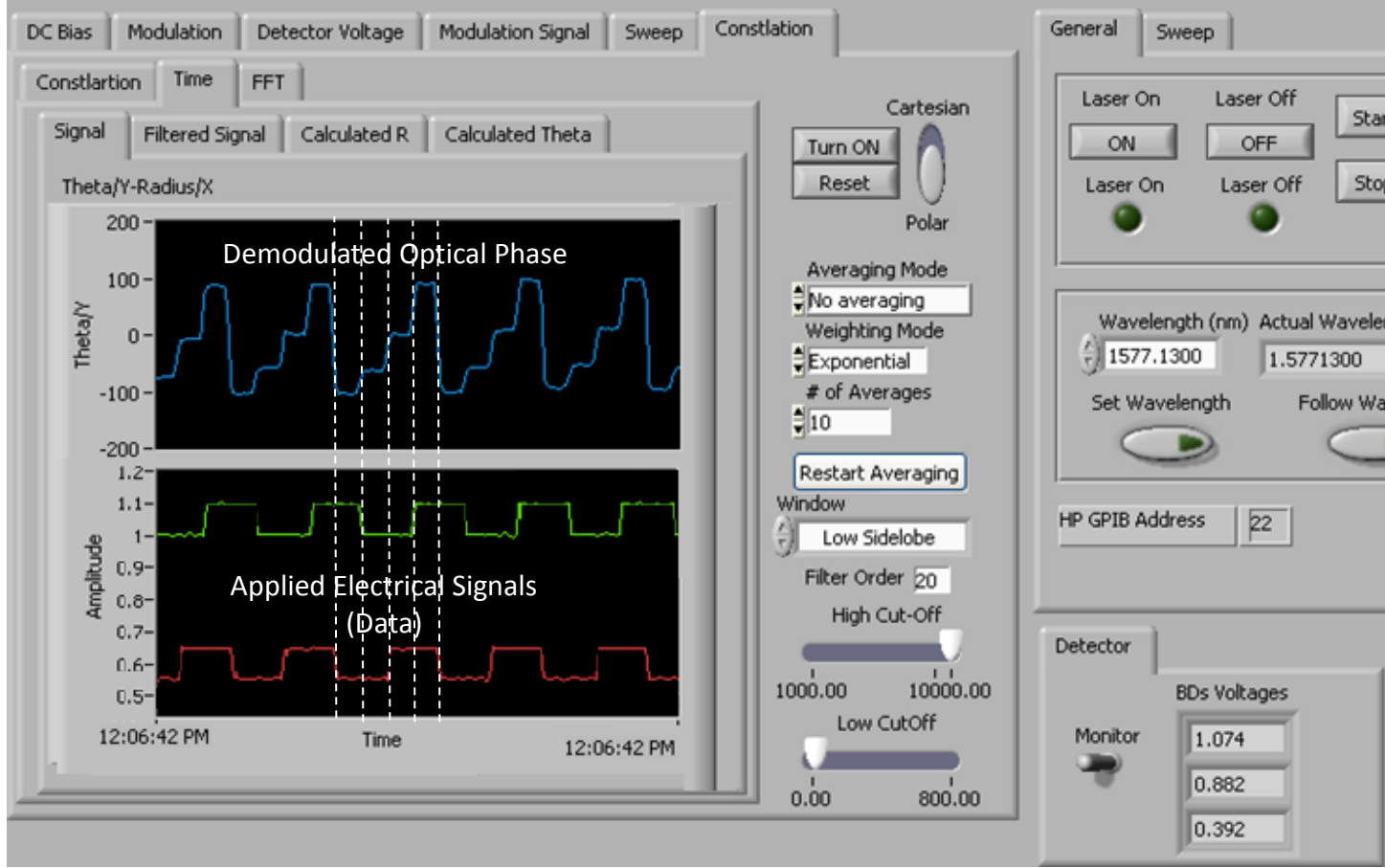


**Figure 9.** Characterization result of the modulator in low frequency. The green and red curves are the electrical signals and the blue curve is the detected phase of the output optical signal.

Figure 9 shows the characterization result of the modulator in low frequency. The green and red curves are the electrical signals and the blue curve is the detected phase of the output optical signal.

### III.D. Design of a high-speed power-efficient modulator for surmounting the constraints imposed by the sensitivity-bandwidth compromise

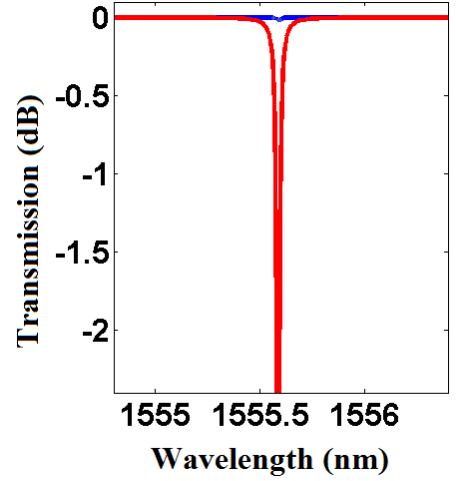
High-speed power-efficient modulators are in large demand for applications in telecommunication, analog signal processing and intra/inter-chip interconnects, and silicon photonics poses to provide for this demand by its high- $Q$  dielectric microresonators. Ultra-high- $Q$  silicon microdisks have large sensitivity to changes in resonance frequency and can in principle be used for low-power modulation. However, there is a well-known compromise between the sensitivity of resonator-based modulators and their operation bandwidth in conventional modulator design approaches based on resonance frequency shift and modulation speed is bound by the microresonator linewidth. Here we present a practical design for a silicon microresonator-based modulator which is not bound by this constraint.

It has been shown that, in a simple modulator structure where a bus waveguide is coupled to a microresonator, modulation of the coupling between the bus waveguide and the microresonator, instead of the modulation of the resonance frequency of the microresonator, would allow

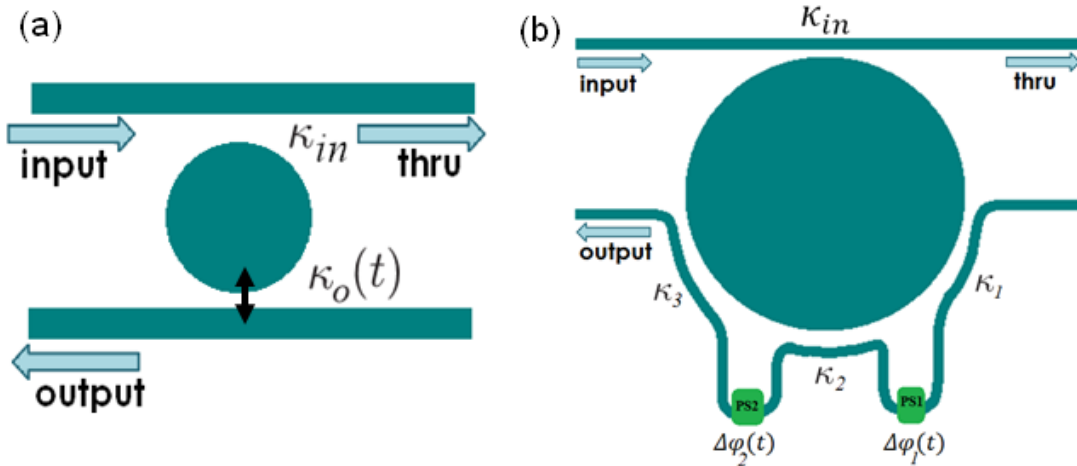
modulating the optical carrier at rates higher than cavity linewidth. Also, for a distortion-free output, particularly at high modulation speeds, the amount of intra-cavity energy should be kept unchanged. Our design is based on this insight into the operation of optical modulators at high modulation rates and provides a practical design for energy-efficient modulation. This design also benefits from keeping the resonance frequency of the microresonator constant which is highly desirable for DWDM applications.

Figure 11(a) shows a schematic illustrating the idea behind this design. Instead of a single bus waveguide coupled to the microresonator, two waveguides are used. The output port waveguide is highly over-coupled to the microresonator cavity and small changes in the coupling would lead to large changes in the output hence energy-efficient or low-power modulation of the output. A practical implementation of this idea is depicted in Figure 11(b). Here, on the output waveguide, two balanced phase-shifters are used which operate anti-symmetrically ( $\delta\phi_1 = -\delta\phi_2$ ) at a bias point of  $\Delta\phi = \pi$  while the couplings are related by  $\kappa_2 = 2\kappa_1\sqrt{1 - \kappa_1^2}$ . Here,  $\kappa_1$  and  $\kappa_2$  are the couplings as indicated on the figure. This particular combination of the phase-shift, bias point and coupling factors lead to constant resonance frequency of the microresonator as seen by the input waveguide and hence constant flow of the carrier into the resonator which reduces the insertion loss significantly and facilitates energy-efficient modulation. This fixed resonance frequency is confirmed as observed in the frequency-domain curve of Figure 10.

Figure 12 shows the time-domain output of the modulator together with the intra-cavity energy dynamics and the small phase-shift required to achieve modulation. It is observed that intra-cavity energy undergoes diminutive fluctuations only and modulation rates as high as 50Gbps for RZ modulation scheme (100Gbps for NRZ modulation) are easily within reach. This modulator has fine performance even when long strings of 1's or 0's are to be transmitted.



**Figure 10.** Frequency-domain transmission response of the proposed modulator. Proper choice of couplings will keep the resonance frequency constant during modulation.



**Figure 11.** (a) Illustration of the design idea. An output waveguide is highly over-coupled to the microresonator and small changes in the coupling lead to large changes in the output thereby enabling power-efficient high-speed



modulation. (b) Schematic of the implementation of the modulator with two balanced phase-shifters that operate anti-symmetrically to keep the resonance frequency of the resonator as seen by the input waveguide intact and guarantee constant flow of the carrier wave into the microresonator thereby leading to significant insertion loss reduction. This design can have modulation rates not bound by the sensitivity-bandwidth trade-off.

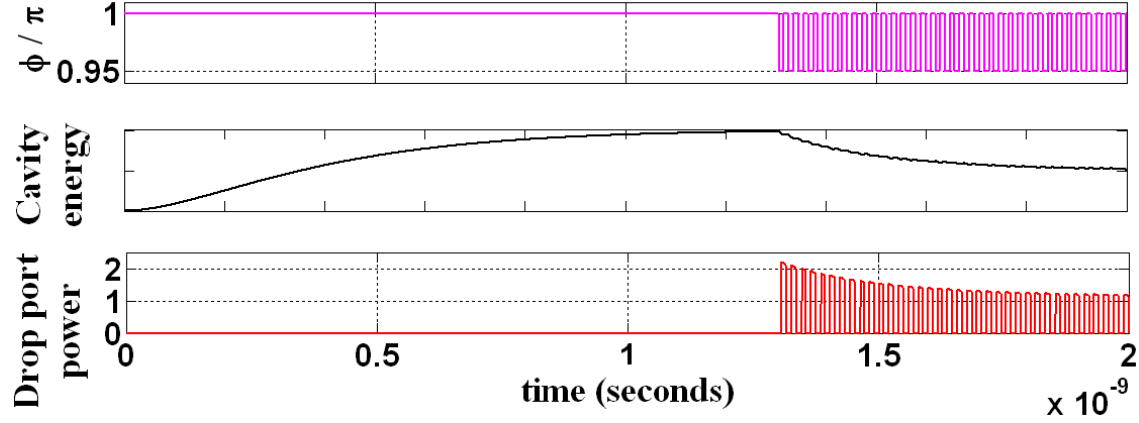


**Figure 12.** Time-domain simulation of the modulated phase (top), intra-cavity energy (middle) and modulated output (bottom) of the modulator of Figure 11(b). Distortion-free high-speed (50Gbps RZ or almost 100Gbps NRZ) modulation with small phase-shift ( $\pi/20$ ) is possible.

The physical design of this modulator has also been investigated and the desired couplings are to be implemented using pulley or concentric coupling of the waveguides with the resonator which has been developed earlier by this group. Figure 13(a) shows finite element method (FEM) simulations of microdisks and waveguides and Figure 13(b) shows curves used to find the length of the pulley coupling portion required to achieve strong coupling to a select mode (here the 3<sup>rd</sup> radial-order mode) of a microdisk or microdonut and not to the neighboring modes (here 2<sup>nd</sup> and 4<sup>th</sup> radial-order modes). Hence the disk and waveguide dimensions as well as coupling lengths could be found for the physical design and fabrication.

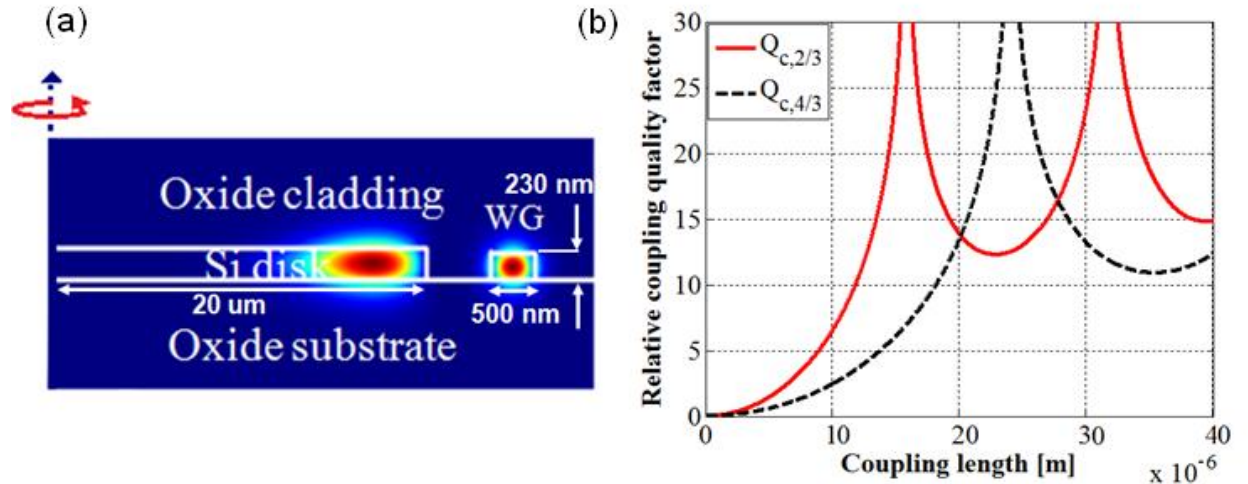


**Figure 13.** Physical design of the proposed modulator: (a) Frequency-domain simulation of a microdisk coupled to a waveguide in a pulley-coupling scheme used to achieve large coupling to select modes of the microresonator. (b) Curves used to find the length of the pulley coupling portion for strong coupling to a select mode (the 3<sup>rd</sup> radial-order mode) of a microdisk and much smaller coupling to the neighboring modes (2<sup>nd</sup> and 4<sup>th</sup> radial-order modes).



### III.E. Reconfigurable reflection canceller for adaptive on-chip optical isolation

So far most of the work on on-chip optical isolation has relied on the use of magneto-optic materials [3]. We demonstrate here a microheater-based reconfigurable SOI device that is capable of achieving optical isolation. The device, shown in Figures 14(a) and 14(b), is composed of a mirror loop with a tunable coupler (the ends of the coupler are connected, thus forming a loop), and a second heater after the loop to change the phase of the optical signal. Another coupler, functioning as an optical tap, is placed at the input to monitor the level of reflection. The unused port of this coupler is terminated by a slow taper, with the purpose of minimizing the level of extra reflection that the tap itself might produce.

The mirror loop acts as a perfect mirror if the tunable coupler is set at its 3-dB point, and as a plain waveguide if the tunable coupler is set to zero. In general, the level of reflection depends on both the coupling ratio and the tunable output phase, as well as the reflected signal at the output port. If this signal is represented by  $r = |r|e^{j\phi_r}$ , and the input signal is represented by  $i$ , the reflected signal at the input port will be:

$$\left[ 2jkt + \frac{r(t^2 - k^2)^2 e^{j2\phi}}{1 - 2jktre^{j2\phi}} \right] i = \left[ 2jk(1 - k^2)^{0.5} + \frac{r(1 - 2k^2)^2 e^{j2\phi}}{1 - 2jk(1 - k^2)^{0.5} r e^{j2\phi}} \right] i,$$

where  $k^2$  is the power coupling ratio of the tunable coupler,  $\phi$  is the tunable phase-shift at the output, and it is assumed that the coupler is lossless ( $t^2 + k^2 = 1$ ). The condition for this expression to equal zero is:

$$r = -2jk(1 - k^2)^{0.5} e^{-j2\phi}.$$

For this to happen, both the amplitude and the phase of the reflection at output are important, and we have two tunable elements to make it possible:

$$2k(1 - k^2)^{0.5} = |r|,$$

$$2\phi = 2n\pi + 3\pi/2 - \phi_r.$$

As can be seen from the equations above, the right value of  $\phi$  has a period of  $\pi$ . Also, for any value of  $|r|$ , there are two possible values of  $k^2$  that are symmetric around 1/2. Since the tunable coupler itself is a Mach-Zehnder interferometer (MZI) consisting of two identical fixed couplers and a tunable phase-shift between the MZI arms,  $k^2$  itself is given by:

$$4\kappa^2(1 - \kappa^2)\cos^2\left(\frac{\phi_{MZI}}{2}\right),$$

where  $\kappa^2$  is the power coupling ratio of each fixed coupler. The maximum of this term is 1, which can only occur if  $\kappa^2 = 1/2$  and  $\phi_{MZI} = 0$ . In practice, because of fabrication imperfections, it is difficult to hit this exact point. However, because of the above-mentioned symmetry, we only need to cover the  $k^2$  range from 0 to 1/2. Therefore, we design the tunable coupler to have a coupling ratio of slightly above 1/2 at  $\phi_{MZI} = 0$ . This also improves the accuracy of our device for a given voltage/current resolution at the driving circuit. Figure 14(c) shows the simulated result for the level of reflection at the input as a function of  $\phi$  and  $k^2$ , when 10% of the output power is reflected with a phase of  $\pi/2$ . Figure 14(d) shows the results of an analogous measurement, along with the measured noise level, with the difference that the x and y axes now show the corresponding heater voltages, and  $k^2$  values span over a range of nearly half the previous one. Also, the z axis is in log scale, and the level of reflection at the output is not necessarily equal to what was assumed in the simulation example.

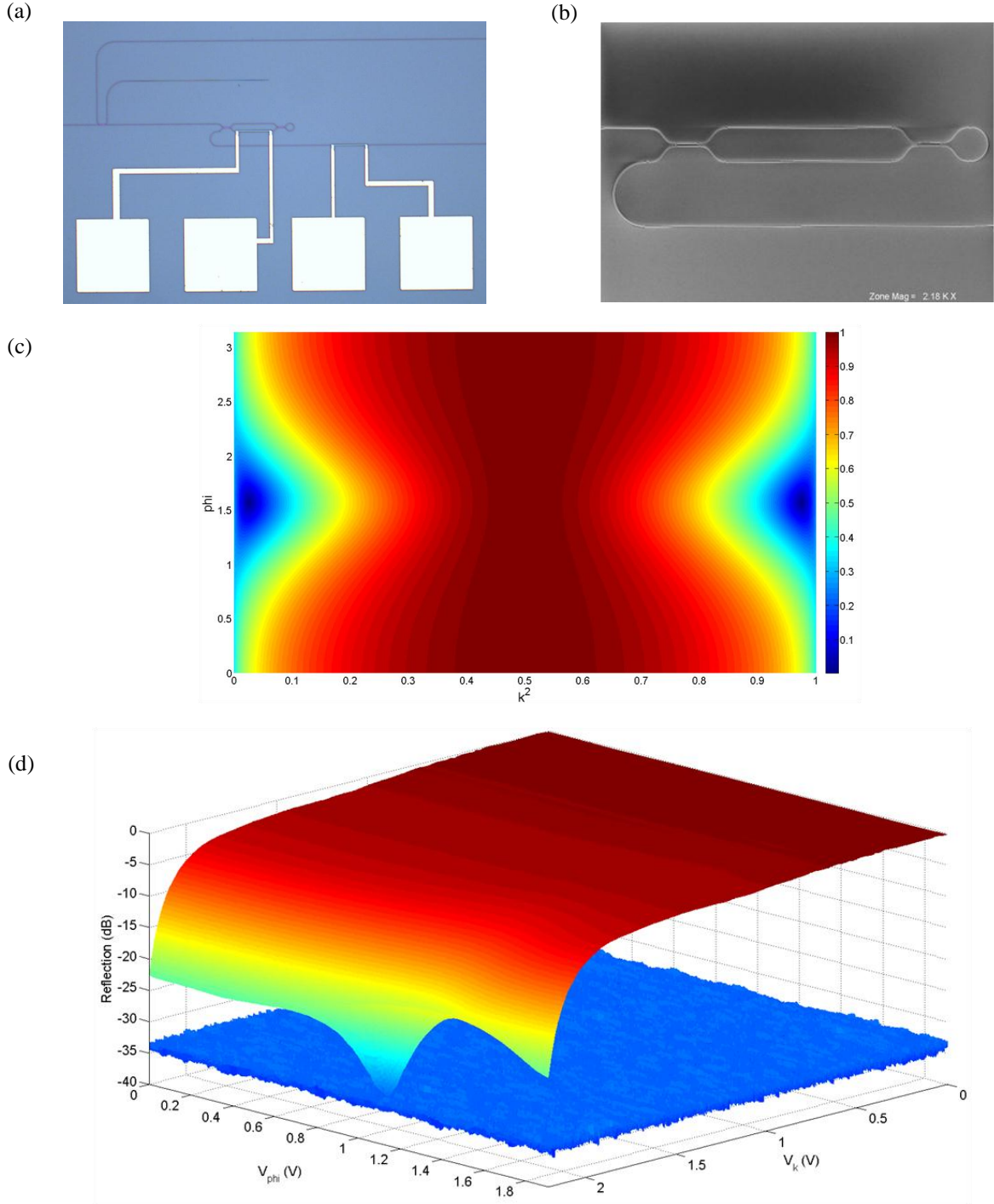


**Figure 14.** (a) Optical micrograph of the tunable reflection canceller. (b) SEM image of the mirror loop. (c) Simulated result for the level of reflection at the input as a function of  $\phi$  and  $k^2$ , when 10% of the output power is reflected with a phase of  $\pi/2$ . (d) Measurement of the back reflection at the input port, as a function of the voltages applied to the coupler and the phase-shift heaters. The reflection hits the noise level (-34 dB) at around  $V_k = 2.15$  V and  $V_{\phi} = 1.1$  V.

### III.F. Demonstration of a 2-input, 2-output reconfigurable cell

Here we demonstrate a reconfigurable SOI-based cell that is capable of receiving two separate input signals and generating any desirable combination of them at a selected output. The input signals are delivered as two orthogonal polarizations on a single input fiber. These two signals are separated by using a 2D grating coupler, designed based on [4], and coupled into the TE modes of two ridge waveguides that act as inputs to the reconfigurable cell. An SEM image of the 2D grating coupler is shown in Figure 15(a). As can be seen from Figure 15(b), this grating is capable of achieving a crosstalk as low as -30 dB between the two arms (when only one of the two orthogonal polarizations is present).

An SEM image of the reconfigurable cell is shown in Figure 15(c). As can be seen in this image, the cell consists of a racetrack resonator that is coupled on each side to one of the input waveguides. The coupling is achieved through a microheater-based MZI tunable coupler, similar to the one discussed in the previous section. The coupler is designed to have a coupling ratio of 100% when  $\phi_{MZI} = 0$ ; therefore, it covers the complete range of coupling ratios from 1 down to 0. The racetrack resonator, with a wavelength-domain FSR of  $\sim 4.2$  nm, enables us to operate on a frequency-selective basis. A microheater is later fabricated above the racetrack, enabling us to shift its resonance to the desired wavelength, and also to compensate the unwanted shifts in wavelength resulting from heater crosstalk and the phase effects of the tunable coupler heaters. A fourth microheater is later fabricated above one of the incoming waveguides in order to compensate or tune the initial phase difference between the two inputs if necessary.

If only one of the orthogonal input polarization channels is active, it is possible to direct this signal to any of the output channels by on/off-switching the lower and upper tunable couplers. Figure 15(d) shows the through transmission of the device for several combinations of the two coupling ratios, when the entire input signal goes into the upper input waveguide. Figure 15(e) shows a similar measurement that is done at the upper output port, i.e., the cross transmission of the device.

Figure 15(f) illustrates that it is possible to combine the two orthogonal incoming polarizations at any desired output channel. These measurements are performed at the lower output port, for a case when the two orthogonal incoming polarizations have equal strength, and as a result, power is equally divided between the upper and lower input waveguides. As can be seen from this figure, the input signals can be both directed to the observed output port, or both directed to the other port resulting in a zero measurement at the observed port. It is also possible to preserve the initial configuration of the signals by turning at least one of the tunable couplers off, resulting in a measurement that is 3 dB lower than the case where the inputs were combined (thus demonstrating the preservation of the equal division of power at the input). The deviations from the -3 dB point are a result of slight initial imbalances between the strength of the two polarizations, as well as the wavelength-dependent behavior of the racetrack.

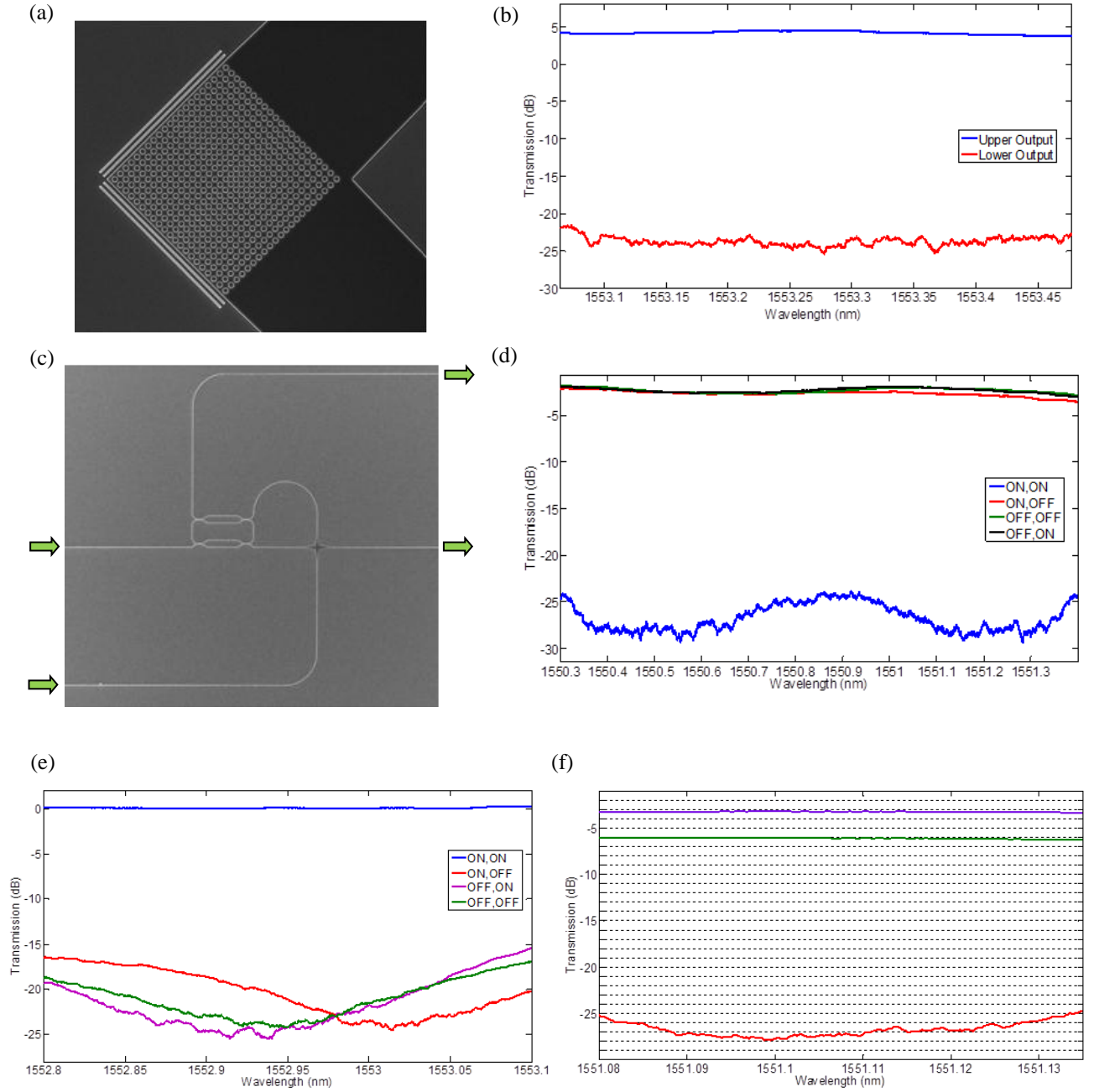


**Figure 15.** (a) SEM image of the 2D grating coupler. (b) Transmission at the two output ports of the 2D grating coupler when only the upper polarization is present. Crosstalk is  $\sim -30$  dB. (c) SEM image of the 2-input, 2-output reconfigurable cell. (d) Through-port transmission of the 2-input, 2-output reconfigurable cell for several combinations of the lower and upper (respectively) coupling ratios, when only the upper polarization channel is present at the input. (e) Cross-port transmission of the 2-input, 2-output reconfigurable cell for several combinations of the lower and upper (respectively) coupling ratios, when only the upper polarization channel is present at the input. (f) Lower output port transmission of the 2-input, 2-output reconfigurable cell when the two orthogonal incoming polarizations have equal strength: Both input channels to the lower output (Purple), Both input channels to the upper output (Red), Unchanged configuration (Green).

### III.G. Development of the double-layer material platform on Si substrate

The proposed multi-layer material platform is developed through oxide-to-oxide bonding of two SOI wafers, as shown in Figure 16. In this process, a thin layer of dielectric material (e.g.,  $\text{Al}_2\text{O}_3$  or  $\text{SiO}_2$ ) is first deposited or grown on both of the SOI wafers and then, the two wafers are bonded together. The Si substrate and its accompanying buried-oxide (BOX) layer on top of the structure are then removed by backside etching to achieve a customized multi-layer Si on insulator (MSOI) wafer, which forms the material system for proposed active devices. The bonding is a critical step as it is important to maintain a thin layer of high-quality dielectric material with uniform thickness to achieve high optical and electrical device performance. This requires careful optimization of the deposition/growth technique of the interface dielectric, rigorous wafer cleaning, surface activation, and bonding parameters (e.g., pressure, duration, and temperature).

#### III.G. (a) Bonding process

SOI wafers used in this work were from Soitec, Inc. with 250nm Si device layer and 3  $\mu\text{m}$  buried oxide layer (BOX). First, a six inch SOI wafer was dry oxidized to reduce the Si device layer to the appropriate thickness (approximately 120 nm). The thermal oxide was not removed at this stage to prevent contamination during wafer cleaving. In addition, the wafer was covered with Red First Contact™ polymer (Photonic Cleaning Technologies, Inc.) to further protect the surface of the wafer from cleaving dust. After cleaving the wafer in 1 inch by 2 inch pieces the protective polymer was peeled off and the top thermal oxide was removed in buffer oxide etchant (BOE). The pieces were then rinsed and blow-dried with  $\text{N}_2$ . Afterwards, 30 nm of dry oxide was thermally grown on the pieces to facilitate the bonding process. After the last oxidation step, each piece was composed of a 30 nm thermal oxide on top of 110 nm of Si device layer on top of 3  $\mu\text{m}$  BOX.

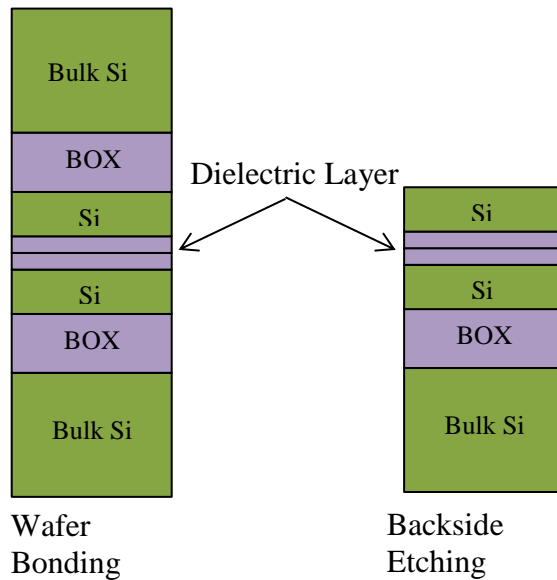


**Figure 16.** Processing of the customized double-layer Si films using wafer bonding and backside etching.

To remove the particles introduced to the surface of SOI pieces in the previous processing steps, we performed a rigorous cleaning to assure void-free and high quality bonded interface. First, we carefully cleaned our glassware in acetone, methanol and isopropyl alcohol (IPA), 30 minutes each. Then, the SOI pieces were cleaned in acetone, methanol and IPA in an ultrasonic bath; each in two steps of 30 minute duration. The next cleaning step was a modified RCA process [Error! Reference source not found.] in which the pieces were first immersed in SC-1 solution ( $\text{H}_2\text{O}:\text{NH}_4\text{OH}:\text{H}_2\text{O}_2$  5:1:1) at  $75^\circ\text{C}$  for 20 minutes, rinsed with DI water, and then immersed in SC-2 solution ( $\text{H}_2\text{O}:\text{HCl}:\text{H}_2\text{O}_2$  6:1:1) at  $75^\circ\text{C}$  for 20 minutes, and finally, rinsed with DI water and blow-dried with  $\text{N}_2$ . High quality quartz beakers were used during SC-1 and SC-2 to reduce contamination from alkali metals from ordinary glassware [Error! Reference source not found.]. After the modified RCA process, 30 seconds of  $\text{O}_2$  plasma was performed on the pieces for surface activation [6], in which we used Plasma-Therm reactive ion etching (RIE) system with  $\text{O}_2$  flow rate of 100 sccm, the chamber pressure of 100 mTorr, and the RF power of 200 W. Immediately after  $\text{O}_2$  plasma exposure, the two pieces were dipped in  $\text{NH}_4\text{OH}$ , to make the surfaces more hydrophilic [0], then, blow dried in  $\text{N}_2$  and placed in contact with each other. The pieces were then bonded in Karl Suss SB6 bonder. After pumping down the bonder chamber pressure to  $5 \times 10^{-5}$  mbar, the bonding pressure was ramped up to 4 bars at room temperature. After 30 minutes, the temperature was ramped up to  $450^\circ\text{C}$  and the sample was held under these conditions for 6 h. This concluded our bonding process. During all of the bonding steps, pieces were only handled from the backside using a vacuum tweezer without touching their front surface. After successful bonding, the bulk Si layer of the top SOI piece was removed using Bosch process. The  $3\text{ }\mu\text{m}$  BOX layer of the top piece was wet etched in BOE, and the optical devices were patterned using electron-beam resist hydrogen silsesquioxane (HSQ). The top and bottom Si layers of the devices were dry etched in  $\text{Cl}_2$  plasma, and the 60 nm dry oxide interface was dry etched in  $\text{CHF}_3/\text{Ar}$  plasma dry. Afterwards, the devices were coated with flowable oxide (FOX<sup>TM</sup>-16 from Dow Corning) as the top cladding material.

### III.G. (b) Characterization

We have demonstrated the viability of achieving high optical-quality double-layer Si material platform by bonding two SOI wafers and fabricating and characterizing basic waveguide and resonator devices. Figure 17 shows the SEM image of the cross-section of a double-layer Si waveguide. Figure 18 shows the transmission spectrum of one of the TE-polarized resonances of a  $20\text{ }\mu\text{m}$  radius microdisk with an intrinsic  $Q$  factor of 500K, which is the highest achieved to date in any double-layer Si structure. Figure 19 shows the transmission spectrum of one of the TE-polarized resonances of a  $2\text{ }\mu\text{m}$  radius microdisk with intrinsic  $Q$  of 17K. This is the most compact high- $Q$  resonator ever developed on a double-layer Si platform and will be the main building block of the ultra-compact switches and modulators in this work. By further optimization of the bonding and fabrication processes, we will further improve the optical quality of the double-layer Si platform.



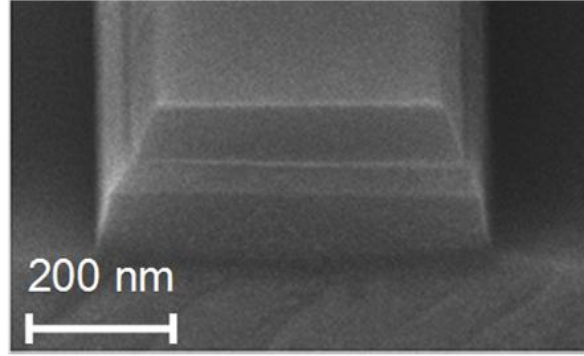


**Figure 17.** SEM image of the cross-section of a double-layer Si waveguide in which each of the two Si layers is 110 nm and the interface oxide is 60 nm thick.

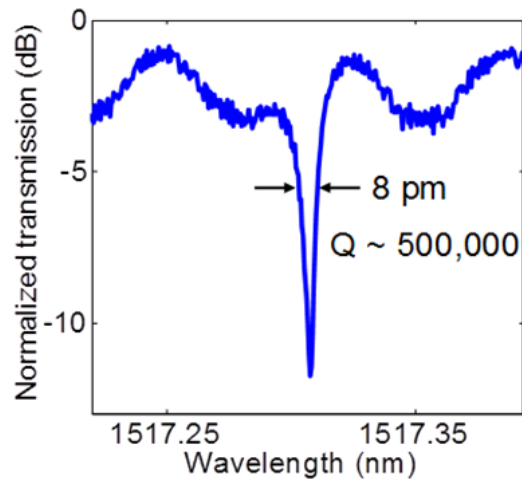


**Figure 18.** The transmission spectrum of one of the TE-polarized resonances of a 20  $\mu\text{m}$ -radius microdisk resonator.

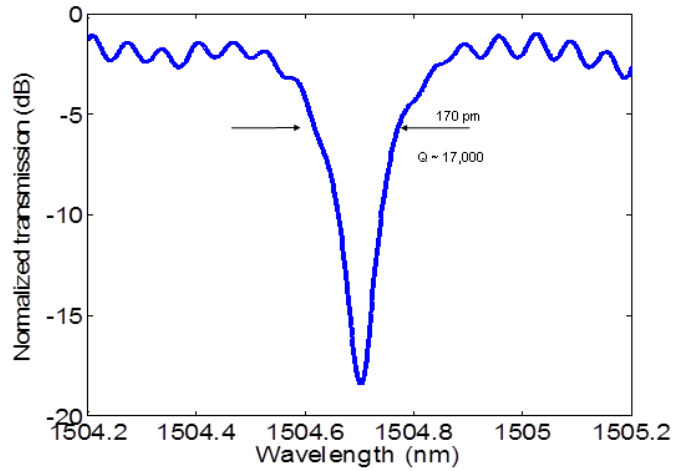


**Figure 19.** The transmission spectrum of one of the TE-polarized resonances of a 2  $\mu\text{m}$ -radius microdisk resonator.

### III.H. New material platform: SiN on Si

Silicon-on-insulator (SOI) technology has received considerable interests in the past decade for integrated photonic circuits. Building blocks such as hybrid silicon lasers, high-speed modulators and switches, hybrid detectors, band-pass filters and optical buffers have been demonstrated. However, no material is perfect and silicon is no exception. For example, for some passive elements such as delay lines, silicon cannot compete with silicon dioxide or silicon nitride in terms of insertion loss and power handling capability for the following two reasons: (1) silicon has a relatively large propagation loss ( $> 0.1$  dB/cm) due to its large refractive index contrast, while in silicon dioxide or silicon nitride, the propagation loss can be one order of magnitude smaller ( $< 0.01$  dB/cm); (2) silicon has strong nonlinear effects, especially, the free carriers generated via the two-photon absorption process can strongly distort the input signal at high power levels, while in silicon dioxide or silicon nitride, the free carriers are absent and nonlinear effects such as the third-order nonlinearity and thermo-optic effect are much weaker. However, active elements such as modulators and phase shifters are difficult to realize in silicon dioxide or silicon nitride platforms due to the difficulty in tuning the refractive index of the host material. Here, we propose a monolithic integration of silicon nitride on silicon-on-insulator platform to enhance the arsenal of photonic circuit designers. The coherent integration of silicon and silicon nitride could generate more powerful devices. Specifically, silicon is perfect for active devices such as modulators and tunable phase shifters. It is also good for passive devices which have a relatively short propagation length, such as couplers. Because of their small sizes (tens of microns), a propagation loss even on the order of 1 dB/cm is acceptable. In addition, because they are either waveguide based or have a very weak power enhancement from the resonating effect, the allowable power is high. For passive components which either require a low-loss performance or a high-power tolerance, silicon nitride becomes a better choice than silicon. For the dense integration, compact silicon nitride microresonators are desired to be incorporated into the SOI platform.

#### III.H. (a) SiN growth, fabrication, and annealing

To achieve the silicon-silicon nitride integration, we first should have the capability to deposit high-quality silicon nitride films on top of the silicon devices. Unlike the work in Ref. [8], where a thin layer of silicon nitride is used to provide weak guiding as waveguides, the silicon nitride layer here has to be thick enough to enable compact microresonators with negligible radiation loss. At telecommunication wavelengths ( $\sim 1.55$   $\mu\text{m}$ ), numerical simulations show that a 400-nm-thick silicon nitride layer permits the realization of a 60- $\mu\text{m}$ -radius microdisk with a radiation  $Q$  more than  $10^{12}$ . However, deposition of a 400-nm-thick silicon nitride layer using the conventional low-pressure chemical vapor deposition (LPCVD) method is not trivial for optical applications. Silicon nitride is well known to have the overtone absorption arising from the N-H bond at the telecommunication wavelength. The content of the hydrogen thus has to be minimized to achieve low-loss performance. As the hydrogen content reduces, however, the stress of the film increases significantly. In fact, low-hydrogen films usually crack at thickness above 200 nm. To solve the problem, a careful balance between the film thickness and material absorption has to be found. Post annealing process has also to be developed to further reduce the hydrogen content so the material absorption loss is eliminated.

Figure 20(a) shows the cross section of the fabricated silicon nitride waveguide for the silicon nitride film grown in the LPCVD furnace available in the cleanroom at Gatech, and Figure 20(b) shows the optical micrograph of a 60- $\mu\text{m}$ -radius microdisk resonator. The blue curve shown in Figure 20(c) shows the transmission measurement of the resonator before the annealing process, and the red curve corresponds to the transmission measurement after the annealing for the same device. As seen from the blue curve, for the wavelength range 1490-1560 nm, the resonance dips are much shallower than those outside of this range, indicating that the material absorption is strong. This absorption spectrum is characteristic of the overtone absorption of the N-H bond. After proper annealing at high temperature (at 1100°C in the nitrogen ambient), the resonance dips become more uniform across the whole wavelength range (red curve), indicating that the hydrogen content has been significantly reduced. Figure 20(d) shows the zoom-in figure for one specific resonance around wavelength 1524 nm. Before the annealing, the absorption-limited  $Q$  is around 150,000, which corresponds to a propagation loss around 4 dB/cm. After the annealing, the  $Q$  dramatically increases to 6,000,000, which corresponds to a propagation loss around 0.1 dB/cm.

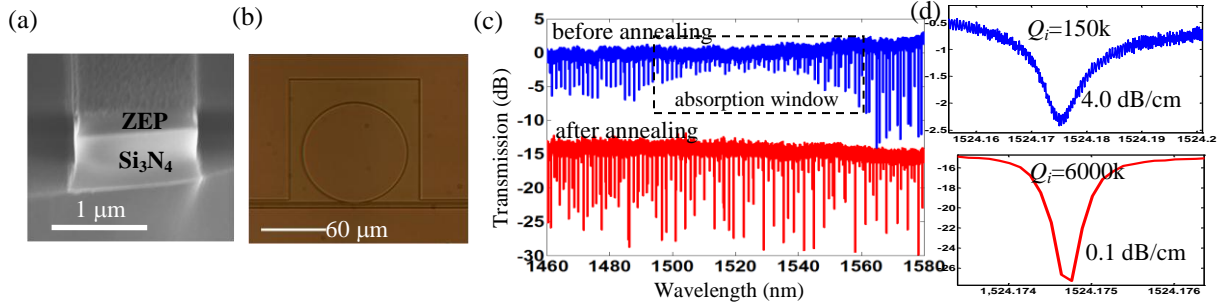


**Figure 20.** (a) Cross section of a silicon nitride waveguide with width of 1.3  $\mu\text{m}$  and height of 400 nm. (b) Optical micrograph of a 60- $\mu\text{m}$ -radius microdisk resonator. (c) Transmission measurements for the resonator shown in (b): blue curve is before annealing and the red curve is after annealing (intentionally moved down by 15 dB for better comparison), for the same microdisk. (d) Zoom-in figures for one resonance around 1524 nm: the upper figure is for the one before annealing and the lower figure is for the one after annealing, for the same microdisk.

### III.H. (b) Integrating SiN to SOI

To enable compact microresonator with a high quality factor ( $Q$ ), thick SiN films have to be grown with a low material absorption loss. At telecommunication wavelengths ( $\sim 1.55 \mu\text{m}$ ), numerical simulations show that a 400-nm-thick SiN layer permits the realization of 60- $\mu\text{m}$ -radius microresonators with radiation  $Q$ s more than  $10^{12}$ . However, deposition of a 400-nm-thick SiN layer using the conventional low-pressure chemical vapor deposition (LPCVD) method is not trivial for optical applications. Particular attention has to be paid to the stress of the SiN film as well as the N-H bond material absorption. Figure 21(a) shows the scanning-electron micrograph (SEM) of the cross section of the fabricated SiN waveguide formed in the SiN film grown in our LPCVD furnace. Electron beam resist ZEP is employed, and the patterning is done using a JBX-9300FS e-beam lithography (EBL) system, followed by plasma etching using the  $\text{CF}_4/\text{CHF}_3$  gas mixture. The integration of SiN to the SOI consists of the following steps: (1) starting with an SOI wafer with a 110-nm-thick Si layer and a 3- $\mu\text{m}$ -thick buried oxide layer; (2) Si devices are fabricated using the HSQ electron beam resist; (3) flowable oxide (FOX<sup>TM</sup>-16) is spin coated, which serves as the buffer layer between the SiN and Si layers. As shown in Figure 21(b), the top surface of the FOX layer is flat, which makes the planarization unnecessary. In

addition, after annealing in the oxygen ambient above 800°C, FOx is converted to SiO<sub>2</sub>, as can be observed from Figure 21(c); (4) 400 nm SiN is deposited by LPCVD, and annealing is performed; (5) SiN microresonators are fabricated, which have to be aligned to the underneath Si waveguides. Figure 21(d) shows that good alignment between the SiN microresonator and the underneath Si waveguide has been achieved; (6) finally, metallic contacts are formed on top of the oxide layer for active tuning of the Si devices.

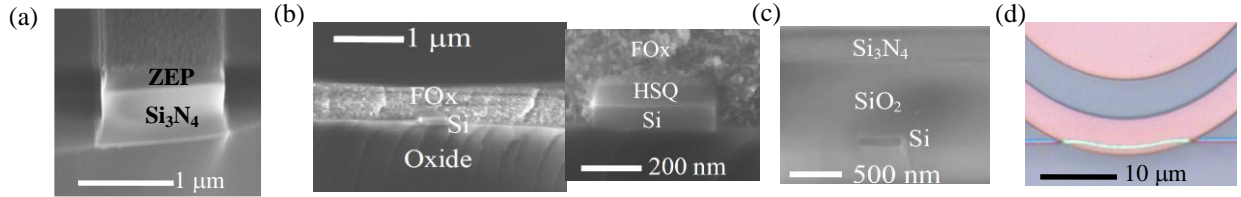


**Figure 21.** (a) SEM showing the cross section of a SiN waveguide with width of 1.3  $\mu\text{m}$  and height of 400 nm. (b) Cross section of the sample after spin-coating FOx. The right figure shows a zoom-in view on the Si waveguide. (c) Cross section of the sample after the FOx annealing and 400 nm SiN deposition. (d) Optical micrograph of coupling region between the SiN microresonator and the underneath Si waveguide.

The first set of fabricated devices includes simple Si waveguide coupled to the SiN microresonator. The Si waveguide width is around 450 nm and the SiN microring has a width of 4  $\mu\text{m}$ . Figure 22(a) illustrates the characterization for the transmission measurement, where the laser signal is sent into the input of the Si waveguide, and collected at the output of the Si waveguide by a detector. Figure 22(b) shows the top view image of the SiN microresonator when it is on resonance (from IR camera), and Figure 22(c) shows the transmission measurement result from the Si waveguide output, where the intrinsic  $Q$ s of the SiN microresonator are measured to be around 1.5 million.

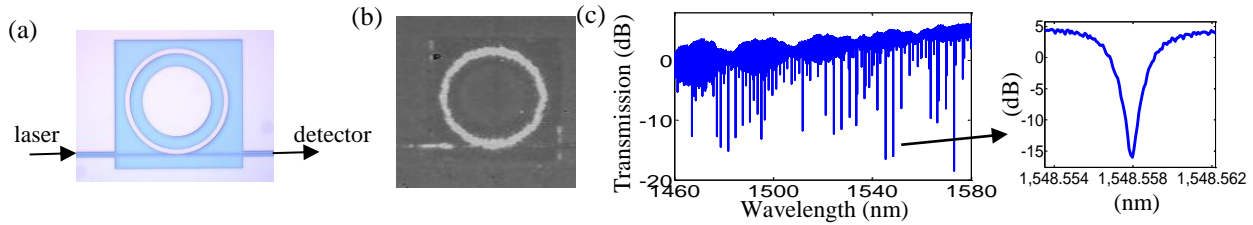


**Figure 22.** (a) Illustration of the transmission measurement. The laser signal is coupled to the input of the Si waveguide and collected at the output of the Si waveguide by a detector. (b) Infrared image of the top view of the SiN microresonator when it is on resonance. (c) Transmission measurement of the SiN microresonator. The graph on the right shows one specific resonance near 1550 nm with an intrinsic  $Q$  around 1.5 million.

## References

- [1] J. Ding, H. Chen, L. Yang, L. Zhang, R. Ji, Y. Tian, W. Zhu, Y. Lu, P. Zhou, R. Min, and M. Yu, "Ultra-low-power carrier-depletion Mach-Zehnder silicon optical modulator," *Opt. Express* **20**, 7081 (2012).
- [2] M. Sodagar, A. H. Atabaki, A. A. Eftekhari, and A. Adibi, "Resonator-based Multichannel DQPSK Optical Modulator on SOI Platform," *Frontiers in Optics (FiO)*, Rochester, NY, Oct. 2012, paper FTu5A.
- [3] L. Bi, J. Hu, P. Jiang, D. H. Kim, G. F. Dionne, L. C. Kimerling, and C. A. Ross, "On-chip optical isolation in monolithically integrated non-reciprocal optical resonators," *Nat. Photon.* **5**, 758 (2011).
- [4] L. Xu, X. Chen, C. Li, and H. K. Tsang, "Bi-wavelength two dimensional chirped grating couplers for low cost WDM PON transceivers," *Opt. Comm.*, **284**, 2242 (2011).
- [5] W. Kern, "Hydrogen peroxide solutions for silicon wafer cleaning," *RCA Eng.* **28**, 99 (1983).

- [6] O. Zucker, W. Langheinrich, M. Kulozik, H. Goebel, "Application of oxygen plasma processing to silicon direct bonding," *Sens. Actuators A, Phys.* **36**, 227 (1993).
- [7] D. Liang, A. W. Fang, H. Park, T. E. Reynolds, K. Warner, D. C. Oakley, and J. E. Bowers, "Low-temperature, strong SiO<sub>2</sub>-SiO<sub>2</sub> covalent wafer bonding for III-V compound semiconductors-to-silicon photonic integrated circuits," *J. Electron. Mater.* **37**, 1552 (2008).
- [8] J. F. Bauters, M. J. R. Heck, D. John, D. Dai, M. C. Tien, J. S. Barton, A. Leinse, R. G. Heideman, D. J. Blumenthal, and J. E. Bowers, "Ultra-low-loss high-aspect-ratio Si<sub>3</sub>N<sub>4</sub> waveguides," *Opt. Express* **19**, 3163 (2011).

## IV. Publications and Presentations

### IV.A. Journal papers

1. B. Momeni, E. Shah Hosseini, and A. Adibi, "Planar photonic crystal microspectrometers in silicon-nitride for the visible range," *Optics Express*, **17**, 17060 (2009).
2. E. Shah Hosseini, S. Yegnanarayanan, A.H. Atabaki, M. Soltani, and A. Adibi, "High Quality Planar Silicon Nitride Microdisk Resonators for Integrated Photonics in the Visible Wavelength Range," *Optics Express*, **17**, 14543 (2009).
3. Q. Li, M. Soltani, S. Yegnanarayanan, and A. Adibi, "Design and demonstration of compact, wide bandwidth coupled-resonator filters on a silicon-on-insulator platform," *Optics Express*, **17**, 2247 (2009).
4. B. Momeni, E. Shah Hosseini, M. Askari, M. Soltani, and A. Adibi, "Integrated photonic crystal spectrometers for sensing applications," *Optics Communications* **282**, 3168 (2009).
5. B. Momeni, S. Yegnanarayanan, M. Soltani, A. Eftekhar, E. Shah Hosseini, and A. Adibi, "Silicon nanophotonic devices for integrated sensing," **Invited Paper**, *Journal of Nanophotonics*, **3**, 031001 (2009).
6. Q. Li, M. Soltani, A. Atabaki, S. Yegnanarayanan, and A. Adibi, "Quantitative modeling of coupling induced resonance frequency shift in microring resonators," *Opt. Express* **17**(26), 2009.
7. S. Yegnanarayanan, M. Soltani, Q. Li, E. S. Hosseini, A. A. Eftekhar, and A. Adibi, "Microresonators in CMOS compatible substrate," **Invited Paper**, *J. Nanosc. Nanotech* **10**, 1508-24 (2010).
8. E. Shah Hosseini, S. Yegnanarayanan, A. Atabaki, M. Soltani, and A. Adibi, "Systematic design and fabrication of high-*Q* pulley-coupled planar silicon nitride microdisk resonators," *Opt. Express* **18**, 2010.
9. A.H. Atabaki, B. Momeni, A. A. Eftekhar, E. Shah Hosseini, S. Yegnanarayanan, and A. Adibi, "Tuning of Resonance-Spacing in a Traveling-Wave Resonator Device," *Opt. Express* **18**, 2010.
10. M. Soltani, S. Yegnanarayanan, Q. Li, and A. Adibi, "Systematic Engineering of Waveguide-Resonator Coupling for Silicon Microring/Microdisk/Racetrack Resonators: Theory and Experiment," *IEEE Journal of Quantum Electron.*, **46**(8), 2010.
11. M. Soltani, Q. Li, S. Yegnanarayanan, and A. Adibi, "Toward ultimate miniaturization of high *Q* silicon traveling-wave microresonators," *Opt. Express* **18**, 19541–19557 (2010).
12. A. H. Atabaki, E. S. Hosseini, A. A. Eftekhar, S. Yegnanarayanan, and A. Adibi, "Optimization of metallic microheaters for high-speed reconfigurable silicon photonics," *Opt. Express* **18**, 18312-18323 (2010).
13. P. Alipour, E. Shah Hosseini, A. A. Eftekhar, B. Momeni, and A. Adibi, "Athermal performance in high-*Q* polymer-clad silicon microdisk resonators," *Opt. Lett.* **35**, 3462–3464 (2010).
14. Q. Li, S. Yegnanarayanan, M. Soltani, P. Alipour, and A. Adibi, "A temperature-insensitive third-order coupled-resonator filter for on-chip terabit/s optical interconnects," *IEEE Photon. Technol. Lett.* **22**, 1768-1770 (2010).
15. P. Alipour, A. A. Eftekhar, A. H. Atabaki, Q. Li, S. Yegnanarayanan, C. K. Madsen, and A. Adibi, "Fully reconfigurable compact RF photonic filters using high-*Q* silicon microdisk resonators," *Opt. Express* **19**, 15899–15907 (2011).

16. M. Soltani, S. Yegnanarayanan, Q. Li, A. A. Eftekhar, and A. Adibi, "Self-sustained gigahertz electronic oscillations in ultrahigh- $Q$  photonic microresonators," *Phys. Rev. A* **85**, 053819 (2012).
17. Q. Li, A. A. Eftekhar, Z. Xia, and A. Adibi, "Azimuthal-order variations of surface-roughness induced mode splitting and scattering loss in high- $Q$  microdisk resonators," *Opt. Lett.* **37**, 1586 (2012).
18. Q. Li, A. A. Eftekhar, P. Alipour, A. H. Atabaki, S. Yegnanarayanan, and A. Adibi, "Low-Loss Microdisk-Based Delay Lines for Narrowband Optical Filters," *IEEE Photon. Technol. Lett.* **24**, 1276–1278 (2012).
19. Q. Li, A. A. Eftekhar, Z. Xia, and A. Adibi, "A unified approach to mode splitting and scattering loss in high- $Q$  whispering-gallery-mode microresonators," Submitted, available in arXiv, <http://arxiv.org/pdf/1205.4448v1.pdf> (2012).
20. M. Soltani, S. Yegnanarayanan, A. A. Eftekhar, and A. Adibi, "Optical trapping of sub-micron scale particles using silicon microdisk resonators," Submitted to *Optics Express*.
21. S. Yegnanarayanan, M. Soltani, B. Momeni, W. Roman, G. Cremona, H. Lu, A. Adibi, "On-chip Integration of Microfluidic Channels with Ultra-high  $Q$  Silicon Microdisk Resonators for Lab-on-a-Chip Sensing Applications," Submitted to *Optics Express*.
22. M. Soltani, Q. Li, S. Yegnanarayanan, and A. Adibi, "High- $Q$  Si Microdisk Resonators in Aqueous Environments," Submitted to *Optics Letters*.
23. M. Soltani, S. Yegnanarayanan, and A. Adibi, "Efficient and Spurious-free Finite-Element Modeling of Three-Dimensional Optical Microresonators with Axial Symmetry," Submitted to *IEEE Microwave and Guided Wave Letters*.
24. A. H. Atabaki, A. A. Eftekhar, S. Yegnanarayanan and A. Adibi, "Ultra-Compact, Low-Power and Fast Thermal Reconfiguration for Large-Scale Silicon Photonics," Submitted to *Optics Express*.
25. M. Miri, A. A. Eftekhar, M. Sodagar, A. Adibi, "Electrostatically-tunable high- $Q$  and low-mode-volume one-dimensional photonic crystal resonators," To be submitted.

#### IV.B. Conference presentations

1. M. Miri, A. A. Eftekhar, M. Sodagar, A. Adibi, "Electrostatically-tunable high- $Q$  and low-mode-volume one-dimensional photonic crystal resonators," in *Photonics West*, San Francisco, Feb 2013.
2. Q. Li, A. A. Eftekhar, A. H. Atabaki, and A. Adibi, "3-D integration of silicon nitride on silicon-on insulator platform," *Conference on Lasers and Electro-Optics (CLEO/QELS)*, San Jose, May 2012.
3. Q. Li, A. A. Eftekhar, M. Sodagar, A. H. Atabaki, and A. Adibi, "Tunable narrowband filters based on SiN-on-SOI platform," *IEEE Photonics Conference*, San Francisco, September 2012.
4. H. Taheri, A. A. Eftekhar, A. H. Atabaki, and A. Adibi, "Low-Power Modulation by Dynamic Control of High- $Q$  Microresonator-Waveguide Coupling," *Rochester, NY*, Oct. 2012, paper FTh2D.
5. M. Sodagar, A. H. Atabaki, A. A. Eftekhar, and A. Adibi, "Resonator-based Multichannel DQPSK Optical Modulator on SOI Platform," *Frontiers in Optics (FiO)*, Rochester, NY, Oct. 2012, paper FTu5A.
6. A. A. Eftekhar, M. Sodagar, H. Moradinejad, A. H. Hosseinnia, Q. Li, A. H. Atabaki, and A. Adibi, "Multi-Layer Material Platforms for Reconfigurable Nanophotonic Structures," *Frontiers in Optics (FiO)*, Rochester, NY, Oct. 2012, paper FW4F.
7. M. Soltani, A. A. Eftekhar, and A. Adibi, "High Frequency Oscillations in Ultra-high  $Q$  Silicon Microresonators," in *Conference on Lasers and Electro-Optics*, OSA Technical Digest (CD) (Optical Society of America, 2011), paper CWC2.
8. A. H. Atabaki, and A. Adibi, "Ultra-Compact Coupled-Resonator Device for Four-Wave-Mixing Applications," in *Conference on Lasers and Electro-Optics*, OSA Technical Digest (CD) (Optical Society of America, 2011), paper CTuS6.
9. A. H. Atabaki, and A. Adibi, "Demonstration of wavelength conversion in a reconfigurable coupled resonator in silicon," in *IEEE Photonics Conference (PHO)*, 399–400 (2011).

10. P. Alipour, A. A. Eftekhar, A. H. Atabaki, Q. Li, S. Yegnanarayanan, C. K. Madsen, and A. Adibi, "Comparison of Cascade, Baseline, and Lattice Architectures for Ultra-Compact RF Photonic Filters on SOI," in Integrated Photonics Research, Silicon and Nanophotonics, OSA Technical Digest (CD) (Optical Society of America, 2011), paper IMD3.
11. P. Alipour, A. A. Eftekhar, A. H. Atabaki, Q. Li, S. Yegnanarayanan, C. Madsen, and A. Adibi, "Optimization of filter architecture for high-order RF-photonic filters on SOI," in IEEE Photonics Conference (PHO), 405–406 (2011).
12. P. Alipour, A. A. Eftekhar, A. H. Atabaki, Q. Li, S. Yegnanarayanan, C. Madsen, and A. Adibi, "Fully Reconfigurable Compact RF Photonic Filters Using High-Q Silicon Microdisk Resonators," in Optical Fiber Communication Conference, OSA Technical Digest (CD) (Optical Society of America, 2011), paper OThM5.
13. M. Soltani, A. H. Atabaki, Q. Li, A. A. Eftekhar, S. Yegnanarayanan, and A. Adibi, "Novel resonance-based silicon nanophotonic structures," in the 10th International Conference on Numerical Simulation of Optoelectronic Devices (NUSOD), Sep 2010..
14. P. Alipour, A. A. Eftekhar, A. H. Atabaki, Q. Li, S. Yegnanarayanan, C. Madsen, and A. Adibi, "Fully reconfigurable compact RF photonic filters using high-Q silicon microdisk resonators," in the 23rd Annual Meeting of the IEEE Photonics Society, 236–237 (2010).
15. P. Alipour, A. A. Eftekhar, A. H. Atabaki, Q. Li, S. Yegnanarayanan, C. Madsen, and A. Adibi, "Compact fully reconfigurable multi-stage RF photonic filters using high-Q silicon microdisk resonators," in the 7th IEEE International Conference on Group IV Photonics (GFP), 368–370 (2010).
16. Q. Li, S. Yegnanarayanan, A. A. Eftekhar, and A. Adibi, "Low-loss microdisk-based delay lines for narrowband optical filters," in Integrated Photonics Research Silicon and Nanophotonics, OSA Technical Digest (CD) (Optical Society of America), paper IMC7, July 2010.
17. A. H. Atabaki, A. A. Eftekhar, S. Yegnanarayanan, and A. Adibi, "Novel micro-heater structure for low-power and fast photonic reconfiguration," in Conference on Lasers and Electro-Optics, OSA Technical Digest (CD) (Optical Society of America, 2010), paper CWP6.
18. A. H. Atabaki, Q. Li, S. Yegnanarayanan, and A. Adibi, "Demonstration of frequency-detuning compensation in a coupled-resonator device for efficient four-wave-mixing," in Conference on Lasers and Electro-Optics, OSA Technical Digest (CD) (Optical Society of America, 2010), paper CThR3.
19. P. Alipour, A. H. Atabaki, A. A. Eftekhar, and A. Adibi, "Titania-Clad Microresonators on SOI With Athermal Performance," in Conference on Lasers and Electro-Optics, OSA Technical Digest (CD) (Optical Society of America, 2010), paper JThE44.
20. P. Alipour, A. H. Atabaki, A. A. Eftekhar, and A. Adibi, "Athermal Performance in Titania-Clad Microring Resonators on SOI," in Integrated Photonics Research, Silicon and Nanophotonics, OSA Technical Digest (CD) (Optical Society of America, 2010), paper IMC6.
21. P. Alipour, A. H. Atabaki, A. A. Eftekhar, and A. Adibi, "Athermal Performance In Titania-clad Microresonators On SOI," in Frontiers in Optics, OSA Technical Digest (CD) (Optical Society of America, 2010), paper FThQ6.
22. M. Soltani, S. Yegnanarayanan, Q. Li, A. H. Atabaki, A. A. Eftekhar and A. Adibi, "Sustained GHz Oscillations in Ultra-high  $Q$  Silicon Microresonators," IEEE Lasers and Electro-Optics Society, (LEOS), 22<sup>nd</sup> Annual Meeting, Belek-Antalya, Turkey, Oct. 2009.
23. M. Soltani, Q. Li, S. Yegnanarayanan, B. Momeni, A. A. Eftekhar and A. Adibi, "Large-scale Array of Small High- $Q$  Microdisk Resonators for On-chip Spectral Analysis," IEEE Lasers and Electro-Optics Society, (LEOS), 22<sup>nd</sup> Annual Meeting, Belek-Antalya, Turkey, Oct. 2009.
24. A. H. Atabaki, A. A. Eftekhar, S. Yegnanarayanan, and A. Adibi, "Sub-Microsecond Thermal Reconfiguration of Silicon Photonic Devices," IEEE Lasers and Electro-Optics Society, (LEOS), 22<sup>nd</sup> Annual Meeting, Belek-Antalya, Turkey, Oct. 2009.
25. A.H. Atabaki, A. A. Eftekhar, S. Yegnanarayanan, and A. Adibi, "Enhancing Thermal Reconfiguration Speed for Silicon Photonics Applications," Integrated Photonics and Nanophotonics



- Research and Applications, IPRNA 2009, (Optical Society of America), Honolulu, Hawaii, 12 July 2009.
26. M. Soltani, Q. Li, S. Yegnanarayanan, and A. Adibi, "Implementation of Single and Coupled Resonator Filters Using Ultimate Miniaturized Silicon Microdisk Resonators," Integrated Photonics and Nanophotonics Research and Applications, Honolulu, Hawaii, July 2009.
  27. M. Soltani, S. Yegnanarayanan, Q. Li, and A. Adibi, "Systematic Engineering of Waveguide-Resonator Coupling for Silicon Microring/Microdisk Resonators," Integrated Photonics and Nanophotonics Research and Applications, Honolulu, Hawaii, July 2009.
  28. P. Alipour, E. Shah Hosseini, A. A. Eftekhar, B. Momeni, and A. Adibi, "Temperature-Insensitive Silicon Microdisk Resonators Using Polymeric Cladding Layers," in Conference on Lasers and Electro-Optics/International Quantum Electronics Conference, OSA Technical Digest (CD) (Optical Society of America, 2009), paper CMAA4.
  29. P. Alipour, E. Shah Hosseini, A. A. Eftekhar, B. Momeni, and A. Adibi, "Athermal Operation in Polymer-Clad Silicon Microdisk Resonators," in Frontiers in Optics, OSA Technical Digest (CD) (Optical Society of America, 2009), paper FWZ2.
  30. S. Yegnanarayanan, M. Soltani, Q. Li, and A. Adibi, "Optimized Silicon Microdisk with High Sensitivity for Label-free Lab-on-a-Chip Sensing Applications," Conference on Lasers and Electro-Optics, CLEO/QELS 2009, Baltimore, Maryland, 31<sup>st</sup> May - 5<sup>th</sup> June 2009.
  31. A. H. Atabaki, S. Yegnanarayanan, and A. Adibi, "Resonance Spacing Tuning in Traveling-wave Resonators," Conference on Lasers and Electro-Optics, CLEO/QELS 2009, Baltimore, Maryland, 31<sup>st</sup> May - 5<sup>th</sup> June 2009.
  32. A. Eftekhar, M. Soltani, S. Yegnanarayanan, and A. Adibi, "Sub-Wavelength Imaging of Optical Modes in Silicon Microdisk Cavities using a Near-Field Probing Technique," Conference on Lasers and Electro-Optics, CLEO/QELS 2009, Baltimore, Maryland, 31<sup>st</sup> May - 5<sup>th</sup> June 2009.
  33. A. H. Atabaki, M. Soltani, A. A. Eftekhar, S. Yegnanarayanan, and A. Adibi, "Optimization of Metallic-microheaters for Reconfigurable Silicon Photonics," Conference on Lasers and Electro-Optics, CLEO/QELS 2009, Baltimore, Maryland, 31<sup>st</sup> May - 5<sup>th</sup> June 2009.
  34. M. Soltani, Q. Li, S. Yegnanarayanan, and A. Adibi, "Ultimate Miniaturization of Single and Coupled Resonator Filters in Silicon Photonics," Conference on Lasers and Electro-Optics, CLEO/QELS 2009, Baltimore, Maryland, 31<sup>st</sup> May - 5<sup>th</sup> June 2009.
  35. Q. Li, M. Soltani, S. Yegnanarayanan, and A. Adibi, "A Compact Wideband Flat-band Filter for Silicon Photonic Applications," Conference on Lasers and Electro-Optics, CLEO/QELS 2009, Baltimore, Maryland, 31<sup>st</sup> May - 5<sup>th</sup> June 2009.
  36. A. Adibi, B. Momeni, S. Yegnanarayanan, M. Soltani, and A. Eftekhar, "Lab-on-a-Chip Sensing using Ultra-Compact Si Nanophotonic Structures," Invited Paper, The IEEE Lasers and Electro-Optics Society (LEOS) Winter Topical Meeting Series on Nanophotonics, Innsbruck, Austria, January 2009.
  37. A. Eftekhar, M. Soltani, S. Yegnanarayanan, and A. Adibi, "Sub-Wavelength Imaging of Optical Modes in Silicon Microdisk Cavities using a Near-Field Probing Technique," The IEEE Lasers and Electro-Optics Society (LEOS) Winter Topical Meeting Series on Nanophotonics, Innsbruck, Austria, January 2009.
  38. E. Shah Hosseini, S. Yegnanarayanan, and A. Adibi, "Ultra-High Quality Factor Silicon Nitride Planar Microdisk Resonators for Integrated Photonics in the Visible Range: A New Coupling Scheme," The IEEE Lasers and Electro-Optics Society (LEOS) Winter Topical Meeting Series on Nanophotonics, Innsbruck, Austria, January 2009.
  39. A. H. Atabaki, Q. Li, S. Yegnanarayanan, M. Chamanzar, E. Shah Hosseini, A. A. Eftekhar, M. Soltani, B. Momeni, and A. Adibi, "Interferometrically-Coupled Traveling-Wave Resonators for Nonlinear Optics Applications," The IEEE Lasers and Electro-Optics Society (LEOS) Winter Topical Meeting Series on Nanophotonics, Innsbruck, Austria, January 2009.